
Atmospheric gas dynamics in the Perseus cluster observed with Hitomi

Hitomi Collaboration* , Felix AHARONIAN^{1,2,3}, Hiroki AKAMATSU⁴, Fumie AKIMOTO⁵, Steven W. ALLEN^{6,7,8}, Lorella ANGELINI⁹, Marc AUDARD¹⁰, Hisamitsu AWAKI¹¹, Magnus AXELSSON¹², Aya BAMBA^{13,14}, Marshall W. BAUTZ¹⁵, Roger BLANDFORD^{6,7,8}, Laura W. BRENNEMAN¹⁶, Gregory V. BROWN¹⁷, Esra BULBUL¹⁵, Edward M. CACKETT¹⁸, Rebecca E. A. CANNING^{6,7}, Maria CHERNYAKOVA¹, Meng P. CHIAO⁹, Paolo S. COPPI^{19,20}, Elisa COSTANTINI⁴, Jelle DE PLAA⁴, Cor P. DE VRIES⁴, Jan-Willem DEN HERDER⁴, Chris DONE²¹, Tadayasu DOTANI²², Ken EBISAWA²², Megan E. ECKART⁹, Teruaki ENOTO^{23,24}, Yuichiro EZOE²⁵, Andrew C. FABIAN²⁶, Carlo FERRIGNO¹⁰, Adam R. FOSTER¹⁶, Ryuichi FUJIMOTO²⁷, Yasushi FUKAZAWA²⁸, Akihiro FURUZAWA²⁹, Massimiliano GALEAZZI³⁰, Luigi C. GALLO³¹, Poshak GANDHI³², Margherita GIUSTINI⁴, Andrea GOLDWURM^{33,34}, Liyi GU⁴, Matteo GUAINAZZI³⁵, Yoshito HABA³⁶, Kouichi HAGINO³⁷, Kenji HAMAGUCHI^{9,38}, Ilana M. HARRUS^{9,38}, Isamu HATSUKADE³⁹, Katsuhiko HAYASHI^{22,40}, Takayuki HAYASHI⁴⁰, Tasuku HAYASHI^{13,22}, Kiyoshi HAYASHIDA⁴¹, Junko S. HIRAGA⁴², Ann HORNSCHEMEIER⁹, Akio HOSHINO⁴³, John P. HUGHES⁴⁴, Yuto ICHINOHE²⁵, Ryo IZUKA²², Hajime INOUE⁴⁵, Shota INOUE⁴¹, Yoshiyuki INOUE²², Manabu ISHIDA²², Kumi ISHIKAWA²², Yoshitaka ISHISAKI²⁵, Masachika IWAI²², Jelle KAASTRA^{4,46}, Tim KALLMAN⁹, Tsuneyoshi KAMAE¹³, Jun KATAOKA⁴⁷, Satoru KATSUDA⁴⁸, Nobuyuki KAWAI⁴⁹, Richard L. KELLEY⁹, Caroline A. KILBOURNE⁹, Takao KITAGUCHI²⁸, Shunji KITAMOTO⁴³, Tetsu KITAYAMA⁵⁰, Takayoshi KOHMURA³⁷, Motohide KOKUBUN²², Katsuji KOYAMA⁵¹, Shu KOYAMA²²,

Peter KRETSCHMAR⁵², Hans A. KRIMM^{53,54}, Aya KUBOTA⁵⁵, Hideyo KUNIEDA⁴⁰, Philippe LAURENT^{33,34}, Shiu-Hang LEE²³, Maurice A. LEUTENEGGER^{9,38}, Olivier LIMOUSIN³⁴, Michael LOEWENSTEIN^{9,56}, Knox S. LONG⁵⁷, David LUMB³⁵, Greg MADEJSKI⁶, Yoshitomo MAEDA²², Daniel MAIER^{33,34}, Kazuo MAKISHIMA⁵⁸, Maxim MARKEVITCH⁹, Hironori MATSUMOTO⁴¹, Kyoko MATSUSHITA⁵⁹, Dan McCAMMON⁶⁰, Brian R. McNAMARA⁶¹, Missagh MEHDIPOUR⁴, Eric D. MILLER¹⁵, Jon M. MILLER⁶², Shin MINESHIGE²³, Kazuhisa MITSUDA²², Ikuyuki MITSUISHI⁴⁰, Takuya MIYAZAWA⁶³, Tsunefumi MIZUNO^{28,64}, Hideyuki MORI⁹, Koji MORI³⁹, Koji MUKAI^{9,38}, Hiroshi MURAKAMI⁶⁵, Richard F. MUSHOTZKY⁵⁶, Takao NAKAGAWA²², Hiroshi NAKAJIMA⁴¹, Takeshi NAKAMORI⁶⁶, Shinya NAKASHIMA⁵⁸, Kazuhiro NAKAZAWA^{13,14}, Kumiko K. NOBUKAWA⁶⁷, Masayoshi NOBUKAWA⁶⁸, Hirofumi NODA^{69,70}, Hirokazu ODAKA⁶, Takaya OHASHI²⁵, Masanori OHNO²⁸, Takashi OKAJIMA⁹, Naomi OTA⁶⁷, Masanobu OZAKI²², Frits PAERELS⁷¹, Stéphane PALTANI¹⁰, Robert PETRE⁹, Ciro PINTO²⁶, Frederick S. PORTER⁹, Katja POTTSCHMIDT^{9,38}, Christopher S. REYNOLDS⁵⁶, Samar SAFI-HARB⁷², Shinya SAITO⁴³, Kazuhiro SAKAI⁹, Toru SASAKI⁵⁹, Goro SATO²², Kosuke SATO⁵⁹, Rie SATO²², Makoto SAWADA⁷³, Norbert SCHARTEL⁵², Peter J. SERLEMTSOS⁹, Hiromi SETA²⁵, Megumi SHIDATSU⁵⁸, Aurora SIMIONESCU²², Randall K. SMITH¹⁶, Yang SOONG⁹, Łukasz STAWARZ⁷⁴, Yasuharu SUGAWARA²², Satoshi SUGITA⁴⁹, Andrew SZYMKOWIAK²⁰, Hiroyasu TAJIMA⁵, Hiromitsu TAKAHASHI²⁸, Tadayuki TAKAHASHI²², Shin'ichiro TAKEDA⁶³, Yoh TAKEI²², Toru TAMAGAWA⁷⁵, Takayuki TAMURA²², Keigo TANAKA⁷⁶, Takaaki TANAKA⁵¹, Yasuo TANAKA^{77,22}, Yasuyuki T. TANAKA²⁸, Makoto S. TASHIRO⁷⁸, Yuzuru TAWARA⁴⁰, Yukikatsu TERADA⁷⁸, Yuichi TERASHIMA¹¹, Francesco TOMBESI^{9,79,80}, Hiroshi TOMIDA²², Yohko TSUBOI⁴⁸, Masahiro TSUJIMOTO²², Hiroshi TSUNEMI⁴¹, Takeshi Go TSURU⁵¹, Hiroyuki UCHIDA⁵¹, Hideki UCHIYAMA⁸¹, Yasunobu UCHIYAMA⁴³, Shutaro UEDA²², Yoshihiro UEDA²³,

Shin'ichiro UNO⁸², C. Megan URRY²⁰, Eugenio URSINO³⁰, Qian H. S. WANG⁵⁶, Shin WATANABE²², Norbert WERNER^{83,84,28}, Dan R. WILKINS⁶, Brian J. WILLIAMS⁵⁷, Shinya YAMADA²⁵, Hiroya YAMAGUCHI^{9,56}, Kazutaka YAMAOKA^{5,40}, Noriko Y. YAMASAKI²², Makoto YAMAUCHI³⁹, Shigeo YAMAUCHI⁶⁷, Tahir YAQOUB^{9,38}, Yoichi YATSU⁴⁹, Daisuke YONETOKU²⁷, Irina ZHURAVLEVA^{6,7}, Abderahmen ZOGHBI⁶²

¹Dublin Institute for Advanced Studies, 31 Fitzwilliam Place, Dublin 2, Ireland

²Max-Planck-Institut für Kernphysik, P.O. Box 103980, 69029 Heidelberg, Germany

³Gran Sasso Science Institute, viale Francesco Crispi, 7 67100 L'Aquila (AQ), Italy

⁴SRON Netherlands Institute for Space Research, Sorbonnelaan 2, 3584 CA Utrecht, The Netherlands

⁵Institute for Space-Earth Environmental Research, Nagoya University, Furo-cho, Chikusa-ku, Nagoya, Aichi 464-8601

⁶Kavli Institute for Particle Astrophysics and Cosmology, Stanford University, 452 Lomita Mall, Stanford, CA 94305, USA

⁷Department of Physics, Stanford University, 382 Via Pueblo Mall, Stanford, CA 94305, USA

⁸SLAC National Accelerator Laboratory, 2575 Sand Hill Road, Menlo Park, CA 94025, USA

⁹NASA, Goddard Space Flight Center, 8800 Greenbelt Road, Greenbelt, MD 20771, USA

¹⁰Department of Astronomy, University of Geneva, ch. d'Écogia 16, CH-1290 Versoix, Switzerland

¹¹Department of Physics, Ehime University, Bunkyo-cho, Matsuyama, Ehime 790-8577

¹²Department of Physics and Oskar Klein Center, Stockholm University, 106 91 Stockholm, Sweden

¹³Department of Physics, The University of Tokyo, 7-3-1 Hongo, Bunkyo-ku, Tokyo 113-0033

¹⁴Research Center for the Early Universe, School of Science, The University of Tokyo, 7-3-1 Hongo, Bunkyo-ku, Tokyo 113-0033

¹⁵Kavli Institute for Astrophysics and Space Research, Massachusetts Institute of Technology, 77 Massachusetts Avenue, Cambridge, MA 02139, USA

¹⁶Smithsonian Astrophysical Observatory, 60 Garden St., MS-4. Cambridge, MA 02138, USA

¹⁷Lawrence Livermore National Laboratory, 7000 East Avenue, Livermore, CA 94550, USA

¹⁸Department of Physics and Astronomy, Wayne State University, 666 W. Hancock St, Detroit, MI 48201, USA

- ¹⁹Department of Astronomy, Yale University, New Haven, CT 06520-8101, USA
- ²⁰Department of Physics, Yale University, New Haven, CT 06520-8120, USA
- ²¹Centre for Extragalactic Astronomy, Department of Physics, University of Durham, South Road, Durham, DH1 3LE, UK
- ²²Japan Aerospace Exploration Agency, Institute of Space and Astronautical Science, 3-1-1 Yoshino-dai, Chuo-ku, Sagami-hara, Kanagawa 252-5210
- ²³Department of Astronomy, Kyoto University, Kitashirakawa-Oiwake-cho, Sakyo-ku, Kyoto 606-8502
- ²⁴The Hakubi Center for Advanced Research, Kyoto University, Kyoto 606-8302
- ²⁵Department of Physics, Tokyo Metropolitan University, 1-1 Minami-Osawa, Hachioji, Tokyo 192-0397
- ²⁶Institute of Astronomy, University of Cambridge, Madingley Road, Cambridge, CB3 0HA, UK
- ²⁷Faculty of Mathematics and Physics, Kanazawa University, Kakuma-machi, Kanazawa, Ishikawa 920-1192
- ²⁸School of Science, Hiroshima University, 1-3-1 Kagamiyama, Higashi-Hiroshima 739-8526
- ²⁹Fujita Health University, Toyoake, Aichi 470-1192
- ³⁰Physics Department, University of Miami, 1320 Campo Sano Dr., Coral Gables, FL 33146, USA
- ³¹Department of Astronomy and Physics, Saint Mary's University, 923 Robie Street, Halifax, NS, B3H 3C3, Canada
- ³²Department of Physics and Astronomy, University of Southampton, Highfield, Southampton, SO17 1BJ, UK
- ³³Laboratoire APC, 10 rue Alice Domon et Léonie Duquet, 75013 Paris, France
- ³⁴CEA Saclay, 91191 Gif sur Yvette, France
- ³⁵European Space Research and Technology Center, Keplerlaan 1 2201 AZ Noordwijk, The Netherlands
- ³⁶Department of Physics and Astronomy, Aichi University of Education, 1 Hirosawa, Igaya-cho, Kariya, Aichi 448-8543
- ³⁷Department of Physics, Tokyo University of Science, 2641 Yamazaki, Noda, Chiba, 278-8510
- ³⁸Department of Physics, University of Maryland Baltimore County, 1000 Hilltop Circle, Baltimore, MD 21250, USA
- ³⁹Department of Applied Physics and Electronic Engineering, University of Miyazaki, 1-1

Gakuen Kibanadai-Nishi, Miyazaki, 889-2192

⁴⁰Department of Physics, Nagoya University, Furo-cho, Chikusa-ku, Nagoya, Aichi 464-8602

⁴¹Department of Earth and Space Science, Osaka University, 1-1 Machikaneyama-cho,
Toyonaka, Osaka 560-0043

⁴²Department of Physics, Kwansai Gakuin University, 2-1 Gakuen, Sanda, Hyogo 669-1337

⁴³Department of Physics, Rikkyo University, 3-34-1 Nishi-Ikebukuro, Toshima-ku, Tokyo
171-8501

⁴⁴Department of Physics and Astronomy, Rutgers University, 136 Frelinghuysen Road,
Piscataway, NJ 08854, USA

⁴⁵Meisei University, 2-1-1 Hodokubo, Hino, Tokyo 191-8506

⁴⁶Leiden Observatory, Leiden University, PO Box 9513, 2300 RA Leiden, The Netherlands

⁴⁷Research Institute for Science and Engineering, Waseda University, 3-4-1 Ohkubo,
Shinjuku, Tokyo 169-8555

⁴⁸Department of Physics, Chuo University, 1-13-27 Kasuga, Bunkyo, Tokyo 112-8551

⁴⁹Department of Physics, Tokyo Institute of Technology, 2-12-1 Ookayama, Meguro-ku, Tokyo
152-8550

⁵⁰Department of Physics, Toho University, 2-2-1 Miyama, Funabashi, Chiba 274-8510

⁵¹Department of Physics, Kyoto University, Kitashirakawa-Oiwake-Cho, Sakyo, Kyoto
606-8502

⁵²European Space Astronomy Center, Camino Bajo del Castillo, s/n., 28692 Villanueva de la
Cañada, Madrid, Spain

⁵³Universities Space Research Association, 7178 Columbia Gateway Drive, Columbia, MD
21046, USA

⁵⁴National Science Foundation, 4201 Wilson Blvd, Arlington, VA 22230, USA

⁵⁵Department of Electronic Information Systems, Shibaura Institute of Technology, 307
Fukasaku, Minuma-ku, Saitama, Saitama 337-8570

⁵⁶Department of Astronomy, University of Maryland, College Park, MD 20742, USA

⁵⁷Space Telescope Science Institute, 3700 San Martin Drive, Baltimore, MD 21218, USA

⁵⁸Institute of Physical and Chemical Research, 2-1 Hirosawa, Wako, Saitama 351-0198

⁵⁹Department of Physics, Tokyo University of Science, 1-3 Kagurazaka, Shinjuku-ku, Tokyo
162-8601

⁶⁰Department of Physics, University of Wisconsin, Madison, WI 53706, USA

⁶¹Department of Physics and Astronomy, University of Waterloo, 200 University Avenue
West, Waterloo, Ontario, N2L 3G1, Canada

- ⁶²Department of Astronomy, University of Michigan, 1085 South University Avenue, Ann Arbor, MI 48109, USA
- ⁶³Okinawa Institute of Science and Technology Graduate University, 1919-1 Tancha, Onna-son Okinawa, 904-0495
- ⁶⁴Hiroshima Astrophysical Science Center, Hiroshima University, Higashi-Hiroshima, Hiroshima 739-8526
- ⁶⁵Faculty of Liberal Arts, Tohoku Gakuin University, 2-1-1 Tenjinzawa, Izumi-ku, Sendai, Miyagi 981-3193
- ⁶⁶Faculty of Science, Yamagata University, 1-4-12 Kojirakawa-machi, Yamagata, Yamagata 990-8560
- ⁶⁷Department of Physics, Nara Women's University, Kitauoyanishi-machi, Nara, Nara 630-8506
- ⁶⁸Department of Teacher Training and School Education, Nara University of Education, Takabatake-cho, Nara, Nara 630-8528
- ⁶⁹Frontier Research Institute for Interdisciplinary Sciences, Tohoku University, 6-3 Aramaki-zaaoba, Aoba-ku, Sendai, Miyagi 980-8578
- ⁷⁰Astronomical Institute, Tohoku University, 6-3 Aramaki-zaaoba, Aoba-ku, Sendai, Miyagi 980-8578
- ⁷¹Astrophysics Laboratory, Columbia University, 550 West 120th Street, New York, NY 10027, USA
- ⁷²Department of Physics and Astronomy, University of Manitoba, Winnipeg, MB R3T 2N2, Canada
- ⁷³Department of Physics and Mathematics, Aoyama Gakuin University, 5-10-1 Fuchinobe, Chuo-ku, Sagami-hara, Kanagawa 252-5258
- ⁷⁴Astronomical Observatory of Jagiellonian University, ul. Orla 171, 30-244 Kraków, Poland
- ⁷⁵RIKEN Nishina Center, 2-1 Hirosawa, Wako, Saitama 351-0198
- ⁷⁶Graduate School of Natural Science & Technology, Kanazawa University, Kakuma-machi, Kanazawa, Ishikawa 920-1192
- ⁷⁷Max-Planck-Institut für extraterrestrische Physik, Giessenbachstrasse 1, 85748 Garching, Germany
- ⁷⁸Department of Physics, Saitama University, 255 Shimo-Okubo, Sakura-ku, Saitama, 338-8570
- ⁷⁹Department of Physics, University of Maryland Baltimore County, 1000 Hilltop Circle, Baltimore, MD 21250, USA

⁸⁰Department of Physics, University of Rome “Tor Vergata”, Via della Ricerca Scientifica 1, I-00133 Rome, Italy

⁸¹Faculty of Education, Shizuoka University, 836 Ohya, Suruga-ku, Shizuoka 422-8529

⁸²Faculty of Health Sciences, Nihon Fukushi University, 26-2 Higashi Haemi-cho, Handa, Aichi 475-0012

⁸³MTA-Eötvös University Lendület Hot Universe Research Group, Pázmány Péter sétány 1/A, Budapest, 1117, Hungary

⁸⁴Department of Theoretical Physics and Astrophysics, Faculty of Science, Masaryk University, Kotlářská 2, Brno, 611 37, Czech Republic

*E-mail: ichinohe@tmu.ac.jp, sueda@astro.isas.jaxa.jp, fujimoto@se.kanazawa-u.ac.jp, shota@ess.sci.osaka-u.ac.jp, Caroline.A.Kilbourne@nasa.gov, kitayama@ph.sci.toho-u.ac.jp, m.markevitch@gmail.com, mcnamara@uwaterloo.ca, naomi@cc.nara-wu.ac.jp, Frederick.S.Porter@nasa.gov, tamura.takayuki@jaxa.jp, tanaka@astro.s.kanazawa-u.ac.jp, wernernorbi@gmail.com

Received ; Accepted

Abstract

Extending the earlier measurements reported in Hitomi collaboration (2016, Nature, 535, 117), we examine the atmospheric gas motions within the central 100 kpc of the Perseus cluster using observations obtained with the Hitomi satellite. After correcting for the point spread function of the telescope and using optically thin emission lines, we find that the line-of-sight velocity dispersion of the hot gas is remarkably low and mostly uniform. The velocity dispersion reaches maxima of approximately 200 km s^{-1} toward the central active galactic nucleus (AGN) and toward the AGN inflated north-western ‘ghost’ bubble. Elsewhere within the observed region, the velocity dispersion appears constant around 100 km s^{-1} . We also detect a velocity gradient with a 100 km s^{-1} amplitude across the cluster core, consistent with large-scale sloshing of the core gas. If the observed gas motions are isotropic, the kinetic pressure support is less than 10% of the thermal pressure support in the cluster core. The well-resolved optically thin emission lines have Gaussian shapes, indicating that the turbulent driving scale is likely below 100 kpc, which is consistent with the size of the AGN jet inflated bubbles. We also report the first measurement of the ion temperature in the intracluster medium, which we find to be consistent with the electron temperature. In addition, we present a new measurement of the redshift to the brightest cluster galaxy NGC 1275.

Key words: galaxies: clusters: individual (Perseus) — X-rays: galaxies: clusters — galaxies: clusters:

1 Introduction

Clusters of galaxies are the most massive bound and virialized structures in the Universe. Their peripheries are dynamically young as clusters continue to grow through the accretion of surrounding matter. Disturbances due to subcluster mergers are found even in relaxed clusters with cool cores (e.g., Markevitch et al. 2001; Churazov et al. 2003; Clarke et al. 2004; Blanton et al. 2011; Ueda et al. 2017). Mergers are expected to drive shocks, bulk shear, and turbulence in the intracluster medium (ICM). Clusters with cool cores also host active galactic nuclei (AGN; Burns 1990; Sun 2009) which inject mechanical energy and magnetic fields into the gas of the cluster cores that drive its motions (e.g., Boehringer et al. 1993; Carilli et al. 1994; Churazov et al. 2000; McNamara et al. 2000; Fabian et al. 2003; Werner et al. 2010). Such AGN feedback may play a major role in preventing runaway cooling in cluster cores (see McNamara & Nulsen 2007; Fabian 2012, for reviews). Knowledge of the dynamics of the ICM will be crucial for understanding the physics of galaxy clusters such as heating and thermalization of the gas, acceleration of relativistic particles, and the level of atmospheric viscosity. It also probes the degree to which hot atmospheres are in hydrostatic balance, which has been widely assumed in cosmological studies using galaxy clusters (see Allen et al. 2011, for review).

Bulk and turbulent motions have been difficult to measure owing to the lack of non-dispersive X-ray spectrometers with sufficient energy resolution to resolve line-of-sight (LOS) velocities. For example, a LOS bulk velocity of 500 km s^{-1} produces a Doppler shift of 11 eV for the Fe XXV He α line at 6.7 keV. Most of the previous attempts using X-ray charge-coupled device (CCD) cameras, with typical energy resolutions of $\sim 150 \text{ eV}$, lead to upper limits or low significance ($< 3\sigma$) detections of bulk motions (e.g., Dupke & Bregman 2006; Ota et al. 2007; Dupke et al. 2007; Fujita et al. 2008; Sato et al. 2008, 2011; Sugawara et al. 2009; Nishino et al. 2012; Tamura et al. 2014; Ota & Yoshida 2016); higher significance measurements were reported only in a few merging clusters (Tamura et al. 2011; Liu et al. 2016).

Upper limits on Doppler broadening were also obtained using the Reflection Grating Spectrometer on board XMM-Newton (RGS; den Herder et al. 2001) with typical values of 200–600 km s^{-1} at the 68% confidence level (Sanders et al. 2010, 2011; Bulbul et al. 2012; Sanders &

* The corresponding authors are Yuto ICHINOHE, Shutaro UEDA, Ryuichi FUJIMOTO, Shota INOUE, Caroline KILBOURNE, Tetsu KITAYAMA, Maxim MARKEVITCH, Brian MCNAMARA, Naomi OTA, Scott PORTER, Takayuki TAMURA, Keigo TANAKA and Norbert WERNER

Fabian 2013; Pinto et al. 2015). As the RGS is slitless, spectral lines are broadened by the spatial extent of the ICM, making it challenging to separate and spatially map the Doppler widths.

The Soft X-ray Spectrometer (SXS; Kelley et al. 2016) on board Hitomi (Takahashi et al. 2016) is the first X-ray instrument in orbit capable of resolving the emission lines in extended sources and measuring their Doppler broadening and shifts. The SXS is a non-dispersive spectrometer with an energy resolution of 4.9 eV full-width at half-maximum (FWHM) at 6 keV (Porter et al. 2016). The SXS imaged the core of the Perseus cluster, the brightest galaxy cluster in the X-ray sky. Previous X-ray observations of this region revealed a series of faint, X-ray cavities around the AGN in the central galaxy NGC 1275 (Boehringer et al. 1993; McNamara et al. 1996; Churazov et al. 2000; Fabian et al. 2000) as well as weak shocks and ripples (Fabian et al. 2003, 2006, 2011; Sanders & Fabian 2007), both suggestive of the presence of gas motions. The SXS performed four pointings in total with a field of view (FOV) of $60 \text{ kpc} \times 60 \text{ kpc}$ each and a total exposure time of 320 ks as shown in figure 1 and table 1. Early results based on two pointings toward nearly the same sky region (Obs 2 and Obs 3) were published in Hitomi Collaboration et al. (2016, hereafter H16). H16 reported that the LOS velocity dispersion in a region 30–60 kpc from the central AGN is $164 \pm 10 \text{ km s}^{-1}$ and the gradient in the LOS bulk velocity across the image is $150 \pm 70 \text{ km s}^{-1}$, where the quoted errors denote 90% statistical uncertainties.

In this paper, we present a thorough analysis of gas motions in the Perseus cluster measured with Hitomi. Updates from H16 include; (i) the full dataset including remaining two offset pointings (Obs 1 and Obs 4) are analyzed to probe the gas motions out to 100 kpc from the central AGN; (ii) the effects of the point spread function (PSF) of the telescope with the half power diameter (HPD) of 1.2 arcmin (Okajima et al. 2016) are taken into account in deriving the velocity maps; (iii) the absolute gas velocities are compared to a new recession velocity of NGC 1275 based on stellar absorption lines; (iv) detailed shapes of bright emission lines are examined to search for non-Gaussianity of the distribution function of the gas velocity; (v) constraints on the thermal motion of ions in the ICM are derived combining the widths of the lines originating from various elements; and (vi) revised calibration and improved estimation for the systematic errors (Eckart et al. 2017) are adopted.

This paper is organized as follows. Section 2 describes observations and data reduction. Section 3 presents details of analysis and results. Implications of our results on the physics of galaxy clusters are discussed in section 4. Section 5 summarizes our conclusions. A new redshift measurement of the central galaxy NGC 1275 is presented in appendix 1 and various systematic uncertainties of our results are discussed in appendix 2. The details of the velocity mapping are shown in appendix 3. Throughout the paper, we adopt standard values of cosmological density parameters, $\Omega_M = 0.3$ and $\Omega_\Lambda = 0.7$, and the Hubble constant $H_0 = 70 \text{ km s}^{-1} \text{ Mpc}^{-1}$. In this cosmology, the angu-

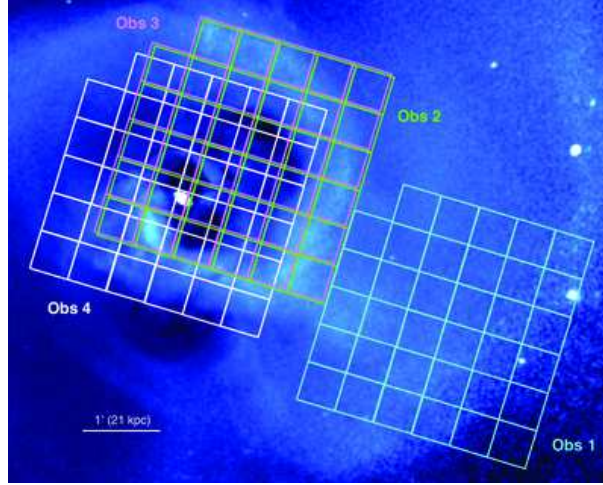


Fig. 1. Hitomi SXS pointings of the Perseus cluster performed during the commissioning phase, overlaid on the Chandra 0.5–3.5 keV band relative deviation image (reproduced from Zhuravleva et al. 2014). The grids correspond to the 6×6 array of the SXS with a lacking corner for the calibration pixel.

Table 1. Summary of the Perseus observations

	ObsID	Observation date	Exposure time (ks)	Pointing direction (RA, Dec) (J2000)
Obs 1	10040010	2016 February 24	48.7	($3^{\text{h}} 19^{\text{m}} 29^{\text{s}}.8, +41^{\circ} 29' 1''.9$)
Obs 2	10040020	2016 February 25	97.4	($3^{\text{h}} 19^{\text{m}} 43^{\text{s}}.6, +41^{\circ} 31' 9''.8$)
Obs 3	10040030, 10040040, 10040050	2016 March 4	146.1	($3^{\text{h}} 19^{\text{m}} 43^{\text{s}}.8, +41^{\circ} 31' 12''.5$)
Obs 4	10040060	2016 March 6	45.8	($3^{\text{h}} 19^{\text{m}} 48^{\text{s}}.2, +41^{\circ} 30' 44''.1$)

lar size of 1 arcmin corresponds to the physical scale of 21 kpc at the updated redshift of NGC 1275, $z = 0.017284$. Unless stated otherwise, errors are given at 68% confidence levels.

2 Observations and data reduction

The Perseus cluster was observed four times with the SXS during Hitomi’s commissioning phase (Obs 1, 2, 3 and 4). A protective gate valve, composed of a $\sim 260 \mu\text{m}$ thick beryllium layer, absorbed most X-rays below 2 keV and roughly halved the transmission of X-rays above 2 keV (Eckart et al. 2016). Figure 1 shows the footprint of the four pointings superposed on the Chandra 0.5–3.5 keV band relative deviation image (reproduced from Zhuravleva et al. 2014). The observations are summarized in table 1. Obs 1 was pointed ~ 3 arcmin east of the cluster core. Obs 2 and Obs 3, covering the cluster core and centered on NGC 1275, are the only observations analyzed in H16. Obs 4 was pointed ~ 0.5 arcmin to south-west of the pointing of Obs 2 and Obs 3.

In order to avoid introducing additional systematic uncertainties into our analysis, we have not applied any additional gain correction adopted in other Hitomi Perseus papers (see e.g. Hitomi Collaboration 2017a, hereafter Atomic paper) unless otherwise quoted. We started the data reduction

from the cleaned event list provided by the pipeline processing version 03.01.005.005 (Angelini et al. 2016) with HEASOFT version 6.21. Detailed description of data screening and additional processing steps are described in Hitomi Collaboration (2017b, hereafter T paper) and elsewhere¹.

3 Analysis and results

In this section, we present the analysis and the results subject-by-subject. Several setups are commonly adopted in most of the analyses unless otherwise stated. The atmospheric X-ray emission was modeled as the emission from a single-temperature, thermal plasma in collisional ionization equilibrium attenuated by the Galactic absorption (TBabs*bapec). The absorbing hydrogen column density was fixed to the value obtained from Leiden/Argentine/Bonn (LAB) survey ($N_{\text{H}} = 0.138 \times 10^{22} \text{ cm}^{-2}$; Kalberla et al. 2005). Willingale et al. (2013) pointed out the effect of the molecular hydrogen column density on the total X-ray absorption, and the effect increases the hydrogen column density by $\sim 50\%$ in the case of Perseus cluster. We however ignored the correction because (i) we do not use the energy below 1.8 keV, where the effect becomes significant, and (ii) the effect is almost only on the continuum parameters, whose effects are second-order and thus negligible in determining the velocity parameters. We ignored the spectral contributions of the cosmic X-ray background (CXB) as they are negligible compared to the emission of the Perseus cluster (Kilbourne et al. 2016). We also ignored the contributions from the non-X-ray background because Hitomi SXS has a significant effective area at high energies (Okajima & Tsujimoto 2017), which makes them negligible compared to the X-ray emission components.

We adopted the abundance table of proto-solar metal of Lodders & Palme (2009) in this paper. Unless otherwise stated, the fitting was performed using XSPEC v12.9.1 (Arnaud 1996) with AtomDB v3.0.9 (Smith et al. 2001; Foster et al. 2012).

The spectra were rebinned so that each energy bin contained at least one event. C-statistics were minimized in the spectral analysis. The redistribution matrix files (RMFs) were generated using the `sxsmkrmf` tool² in which we incorporated the electron loss continuum channel into the redistribution (extra-large-size RMF; Leutenegger et al. 2016)³. Point source ARFs (auxiliary response file) were generated in the 1.8–9.0 keV band using the `aharfgen` tool⁴ at source coordinates (RA, Dec)=($3^{\text{h}}19^{\text{m}}48^{\text{s}}.1$, $+41^{\circ}30'42''$) (J2000).

¹ “The HITOMI Step-By-Step Analysis Guide version 5; <https://heasarc.gsfc.nasa.gov/docs/hitomi/analysis/>

² <https://heasarc.gsfc.nasa.gov/lheasoft/ftools/headas/sxsmkrmf.html>

³ For the analyses shown in the main text. We instead used large-size RMFs for the analyses presented in appendices for computational efficiency. The changes in the best-fit values due to the RMF difference are typically less than a few %.

⁴ <https://heasarc.gsfc.nasa.gov/ftools/caldb/help/aharfgen.html>

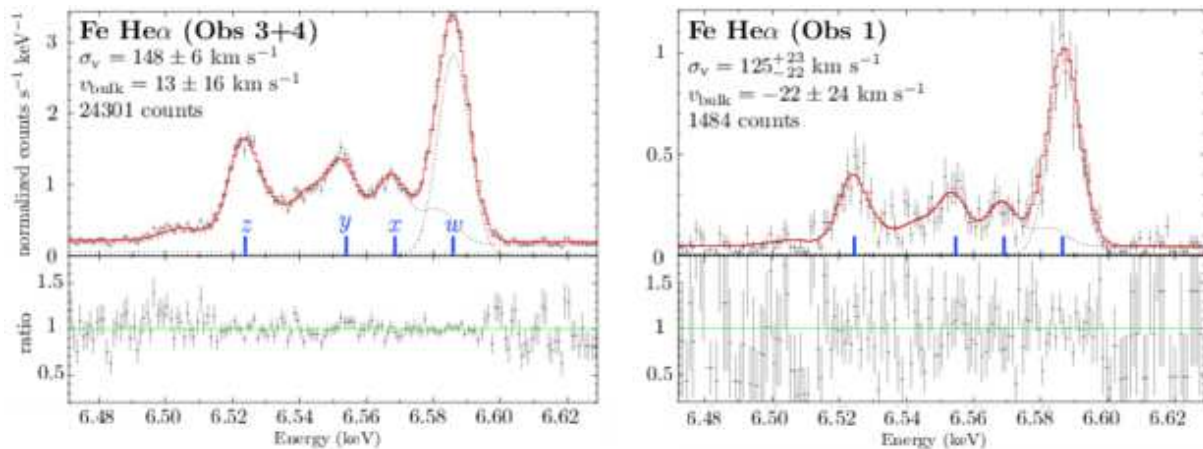


Fig. 2. Fe He α lines of the full-FOV data of Obs 3+Obs 4 (left) and Obs 1 (right). The LOS velocity dispersion (σ_v , w -line excluded. See also table 2), the bulk velocity calculated with respect to the redshift of NGC 1275 (v_{bulk}) and the total number of photons in the displayed energy band are shown in each figure. The red curves are the best-fitting models, and the dotted curves are the spectral constituents, i.e., modified APEC or Gaussian. See main text for details. The energy bin size is 1 eV or wider for lower count bins. The resonance line (w), the intercombination lines (x and y), and the forbidden line (z) are denoted. The letters are as given in Gabriel (1972).

Hereafter in this paper, we distinguish various kinds of line width using the following notations: $\sigma_{v+\text{th}}$ is the observed line width with only the instrumental broadening subtracted; σ_v is the line width calculated by subtracting both the thermal broadening (σ_{th}) and the instrumental broadening from the observed line width (i.e., LOS velocity dispersion). Unless stated otherwise, σ_{th} is computed assuming that electrons and ions have the same temperature. The analysis without this assumption is presented in section 3.4.

3.1 Profiles of major emission lines

In this section, we show observed line profiles of bright transitions and demonstrate qualities of these measurements. The data of Obs 2 were not used in this section and in section 3.2, since Obs 2 (and Obs 1) contains a previously known systematic uncertainty in the energy scale, and the almost identical pointing direction to that of Obs 2's is covered by Obs 3. In figure 2 we show the Fe He α emission line complex from Obs 3+Obs 4, and Obs 1. The panels in figure 3 show S Ly α , Fe Ly α and Fe He β lines of Obs 3+Obs 4. The figures indicate the best-fitting LOS velocity dispersions (σ_v) and bulk velocities calculated with respect to the new stellar absorption line redshift measurement of NGC 1275 ($v_{\text{bulk}} \equiv (z - 0.017284)c_0 - 26.4 \text{ km s}^{-1}$, where c_0 is the speed of light, $z = 0.017284$ is the redshift of NGC 1275, and -26.4 km s^{-1} is the heliocentric correction. See also appendix 1 for the redshift measurement). The net photon count is also indicated.

The best-fitting parameters were obtained as follows: We extracted spectra from the event

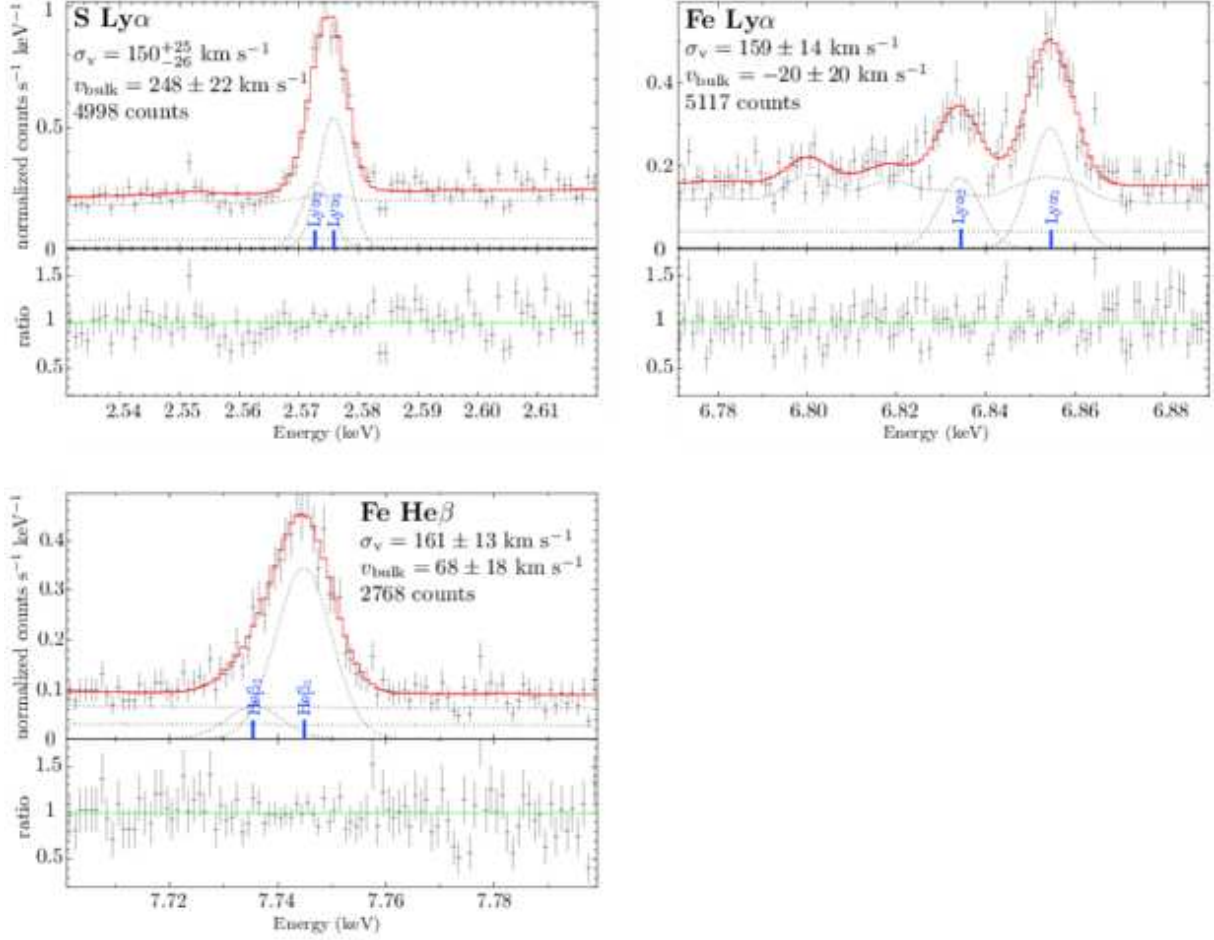


Fig. 3. Same as figure 2, but for S Ly α (upper left), Fe Ly α (upper right) and Fe He β (lower left) of Obs 3+4. Representative line are denoted in the figures.

file (no additional gain correction applied) for the entire FOVs of Obs 3, Obs 4, and Obs 1, and we combined the spectra of Obs 3 and Obs 4. The spectral continua were modeled using a wider energy band of 1.8–9.0 keV using *bapec*, and the obtained continuum parameters were used in the subsequent fitting for extracting the parameter values associated with spectral lines performed in narrower energy bands displayed in figures 2 and 3. In the *bapec* modelling, Fe He α *w* was manually excluded from the atomic database and substituted by an external Gaussian, to minimize the effect of resonance scattering (most pronounced for Fe He α *w*, see Hitomi Collaboration 2017c, hereafter RS paper). In the spectral line modelling, Fe He α *w*, Ly α_1 and Ly α_2 , He β_1 and He β_2 , and S Ly α_1 and Ly α_2 were manually excluded from the atomic database and substituted by external Gaussians. For an Fe Ly α feature, the widths of the two Gaussians were linked to each other, while for Fe He β and S Ly α features, the relative centroid energies and the relative normalizations of each of the two Gaussians were also fixed to the database values.

We investigated the effects of the Fe He α resonance line (*w* line) and the energy scale correc-

Table 2. LOS velocity dispersions of gas motions, obtained from the Fe He α line of Obs 3+Obs 4 data.

	Unit	Without z -correction	With z -correction*
σ_v of w	(km s $^{-1}$)	171 $^{+4}_{-3}$	161 \pm 3
σ_v excluding w	(km s $^{-1}$)	148 \pm 6	144 \pm 6

* z -correction is an additional gain alignment among the detector pixels. See also the text.

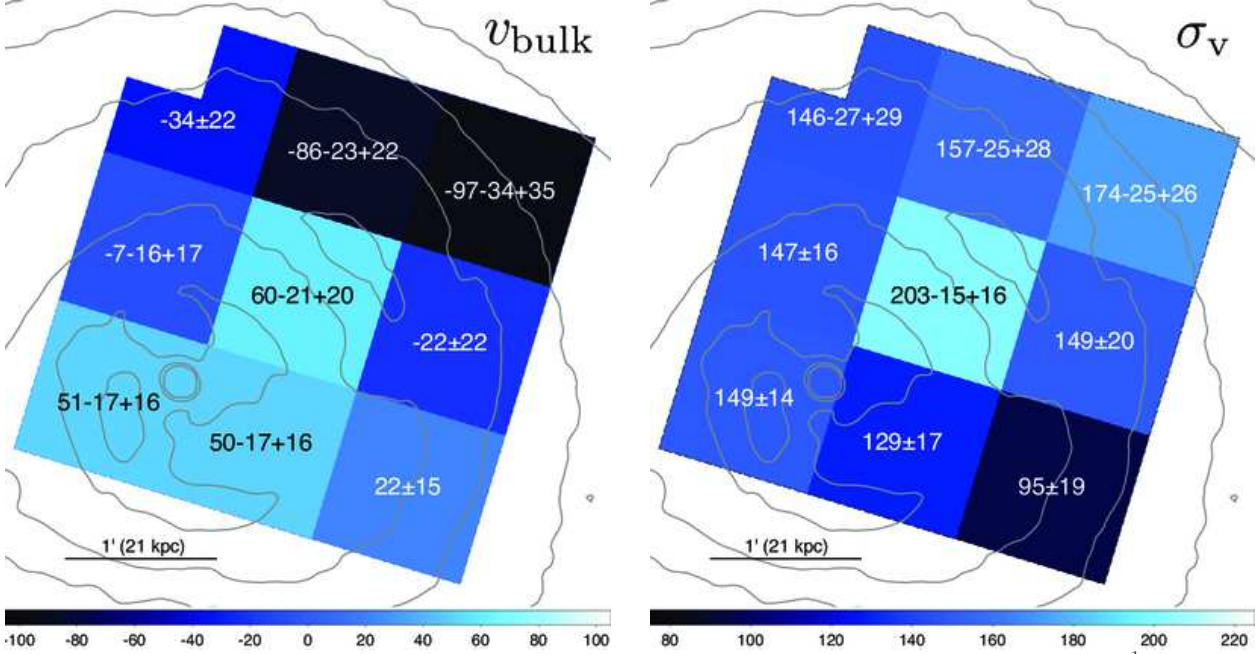


Fig. 4. Benchmark velocity maps. *Left:* bulk velocity (v_{bulk}) map with respect to $z = 0.017284$ (heliocentric correction of -26.4 km s $^{-1}$ applied). *Right:* LOS velocity dispersion (σ_v) map. The unit of the values is km s $^{-1}$. Chandra X-ray contours are overlaid. The best-fitting value is overlaid on each region. Only Obs 3 is used and PSF correction is not applied.

tion on the measured σ_v . Table 2 shows the LOS velocity dispersion (σ_v) measured with or without z -correction – a rescaling of photon energies for individual SXS pixels in order to force the Fe He-alpha lines align, which has been employed in H16 and Aharonian et al. (2017) to cancel out most pixel-to-pixel calibration uncertainties, but which also removes any true LOS velocity gradients. The value of σ_v obtained with the w line is higher than that without the w line, which provides a hint of resonance scattering (see RS paper for details).

3.2 Velocity maps

Firstly, we extracted the benchmark velocity maps by objectively dividing the 6 pixel \times 6 pixel array into 9 subarrays of 2 \times 2 pixels and fitted the spectrum of each region independently, in order to compare the effects of the difference in software and data pipeline versions between H16 and this paper. All model parameters apart from the hydrogen column density were allowed to vary. Only Obs 3 was used for the benchmark maps and the fitting was done using a narrow energy range of 6.4–

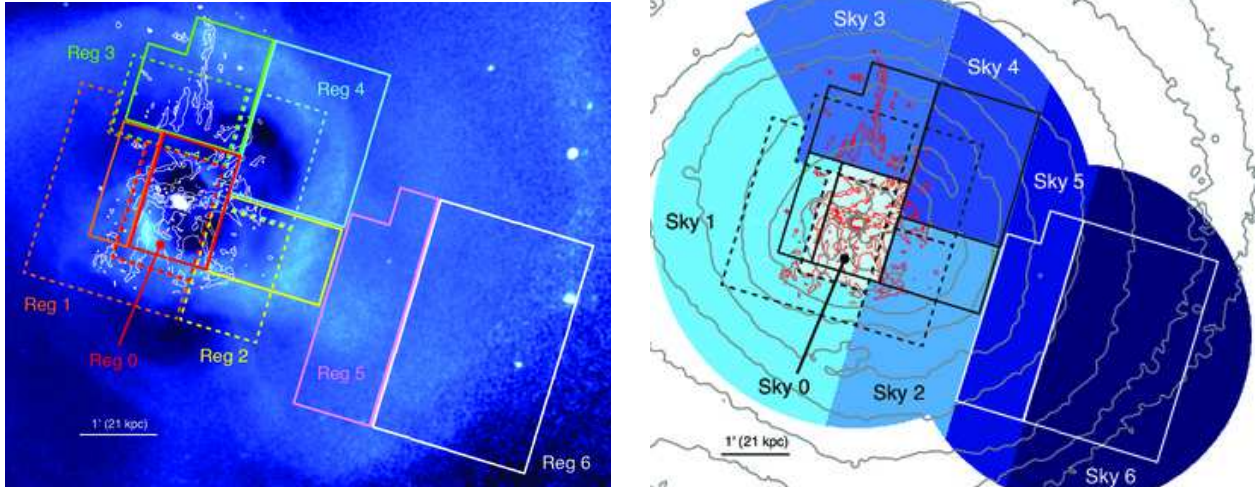


Fig. 5. The regions used for the velocity mapping. *Left:* distinct regions defined by discrete pixels are identified by color coding and number and overlaid on the Chandra relative deviation image. *Right:* the corresponding regions when PSF is taken into account. The Chandra X-ray contours are overlaid. $H\alpha$ contours (Conselice et al. 2001) are also overlaid in white (left) or red (right). The solid-lined polygons are the regions associated with Obs 1 or Obs 3, and the dashed-lined polygons are the regions associated with Obs 4. See also figure 1.

6.7 keV, excluding the energy band corresponding to the resonance line of Fe $He\alpha$ in the observer-frame (6.575–6.6 keV) to avoid the systematics originating from the possible line broadening due to the resonant scattering effect. Figure 4 left shows the bulk velocity (v_{bulk}) map with respect to $z = 0.017284$ (heliocentric correction of -26.4 km s^{-1} applied) and figure 4 right shows the LOS velocity dispersion (σ_v) map. We found a similar trend to the H16 results.

Secondly, we extracted the velocity maps from the regions associated with physically interesting phenomena. Figure 5 shows the regions used for the velocity mapping. Most of the regions correspond to a specific feature pointed out in the literature (e.g. Churazov et al. 2000; Fabian et al. 2006; Salomé et al. 2011): Reg 0 represents the central AGN and the cluster core; Reg 3 covers the northern filaments; and Reg 4 surrounds the northwestern ghost bubble. We excluded Obs 2 in our velocity mapping to avoid potential systematic uncertainties (see appendix 2.1 for details).

The PSF of the telescope (1.2 arcmin HPD) is rather broad, and thus X-ray photons are scattered out of the FOV and into adjacent regions. Also conversely, photons from outside the detector array’s footprint are scattered into the array.

In order to account for the scattering from outside the detector array’s footprint, we extended the sky areas for Reg 1 and Reg 2 to a radius of $r = 3$ arcmin from the central AGN. We extended Reg 3, 4, and 5 to a radius of 3.5 arcmin from the central AGN. Reg 5 and 6 were likewise extended to a radius of 2.5 arcmin from the center of the FOV of Obs 1. Reg 2 included a part of the region of the $r < 2.5$ arcmin circle and Reg 5 also included a part of the region of the $r < 3.5$ arcmin circle. Sky regions are shown in the right panel of figure 5. As the level of PSF blending from outside these

Table 3. Ratio of PSF blending effect on each integration region in the 6.4–6.7 keV band in units of percent.

		Sky region						
		Sky 0	Sky 1	Sky 2	Sky 3	Sky 4	Sky 5	Sky 6
Integration region	Reg 0 Obs 3	62.3	10.1	13.8	7.4	6.1	0.4	0.1
	Reg 0 Obs 4	64.2	16.6	10.2	5.4	3.2	0.3	0.1
	Reg 1 Obs 3	43.9	43.3	3.0	8.3	1.2	0.2	0.1
	Reg 1 Obs 4	22.1	67.2	4.3	5.5	0.7	0.2	0.1
	Reg 2 Obs 3	10.2	2.8	65.5	1.5	12.0	7.6	0.5
	Reg 2 Obs 4	17.8	6.5	66.5	1.5	5.7	1.9	0.2
	Reg 3 Obs 3	12.7	6.8	2.5	63.6	13.9	0.5	0.1
	Reg 3 Obs 4	22.7	15.7	2.9	51.3	7.0	0.3	0.1
	Reg 4 Obs 3	8.2	1.8	12.6	8.5	61.5	6.8	0.5
	Reg 4 Obs 4	17.5	2.4	16.4	12.6	48.9	2.0	0.2
	Reg 5 Obs 1	1.3	0.9	17.5	0.4	4.0	60.8	15.0
	Reg 6 Obs 1	0.8	0.8	4.4	0.4	1.6	16.0	75.9

Sky regions correspond to the regions shown in the right panel of figure 5 and integration regions are associated with the regions indicated in the left panel of figure 5. The fractions of photons coming from each sky region to one integration region appear in the same row. The level of PSF blending from outside these regions was found to be less than 1 % and not listed in the table. For example, Reg 1 Obs 3 is strongly affected by scattered photons from Sky 0, and the contamination from Sky 0 to Reg 5 or Reg 6 is almost zero.

regions was found to be less than 1 %, we ignored them. We assumed a uniform plasma properties within each sky region.

In order to model all the spectra simultaneously, we estimated the relative flux contributions from all the sky regions (figure 5 right) to every single integration region (figure 5 left). We measured the quantity of PSF scattering from inside or outside the corresponding sky using `aharfgen`. For the input, we used the deep Chandra image in the broad band of 1.8–9.0 keV and an image in the 6.4–6.7 keV including the line emission only (see appendix 3). We show a matrix of its effect in the 6.4–6.7 keV band in table 3. We also checked its effect in the 1.8–9.0 keV band. The trend in the 1.8–9.0 keV band is consistent with that in the 6.4–6.7 keV band.

In order to determine ICM velocities, we fitted spectra from all regions simultaneously, taking scattering into account (see appendix 3.1 for technical details). We first obtained the PSF-corrected values of the temperature, Fe abundance and normalization of each region. This fitting was done in the energy range of 1.8–9.0 keV, excluding the narrow energy range of 6.4–6.7 keV, and the AGN contribution to the spectra was included using the model shown in Hitomi Collaboration (2017d, hereafter

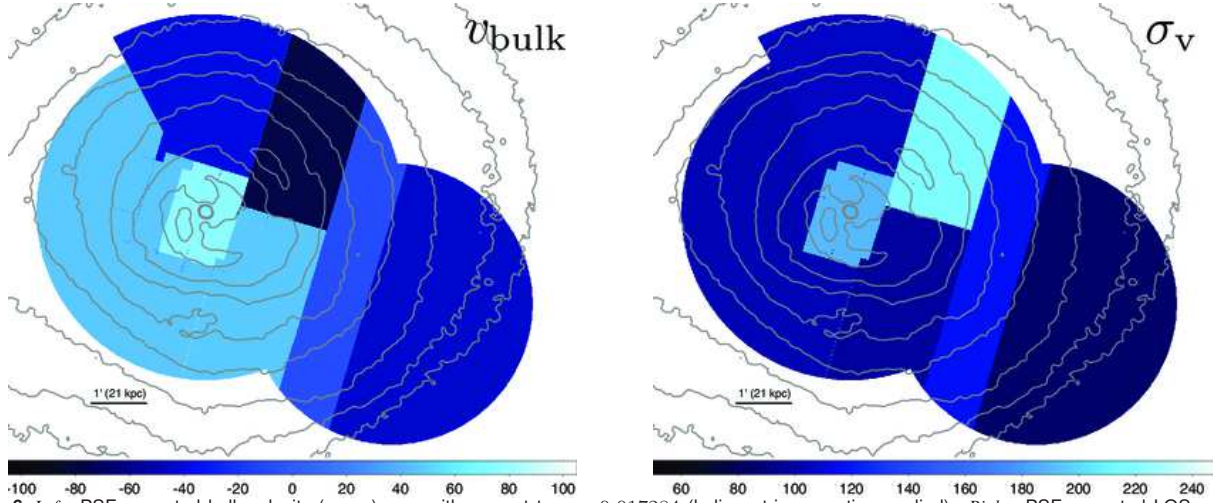


Fig. 6. *Left*: PSF corrected bulk velocity (v_{bulk}) map with respect to $z = 0.017284$ (heliocentric correction applied). *Right*: PSF corrected LOS velocity dispersion (σ_v) map. The unit of the values is km s^{-1} . The Chandra X-ray contours are overlaid.

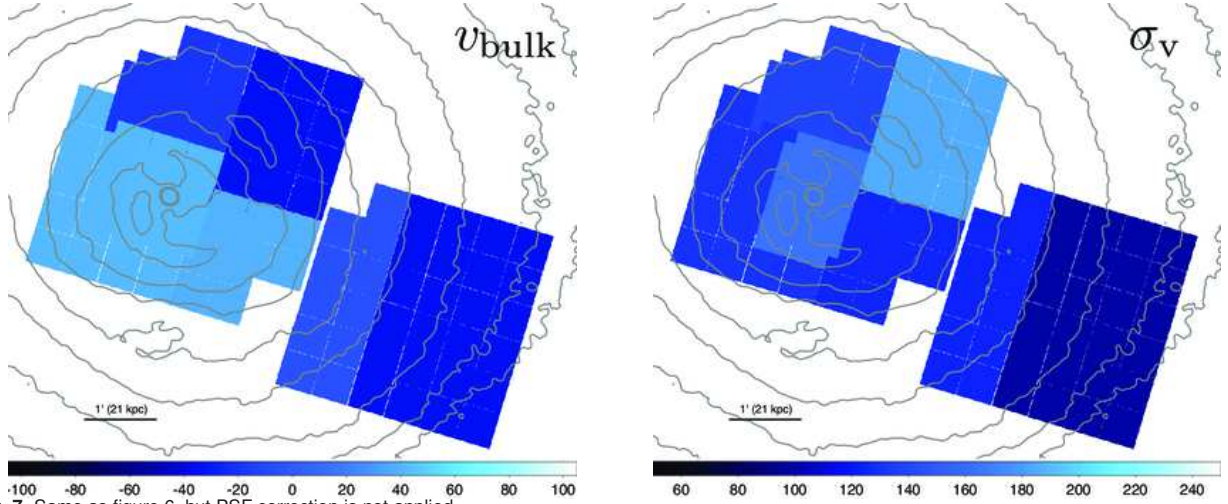


Fig. 7. Same as figure 6, but PSF correction is not applied.

AGN paper), after convolution with the point source ARFs. The velocity width and redshift of each plasma model were fixed to 160 km s^{-1} and 0.017284 respectively. The obtained C-statistic/d.o.f. (degree of freedom) in the continuum fitting is $63146.77/68003$. Detailed description of the measurement of the continuum parameters are shown in AGN paper and T paper.

After determining the self-consistent parameter set of the continuum as mentioned above, we again fitted all the spectra simultaneously to obtain the parameters associated with spectral lines. This time, the temperatures and normalizations were fixed to the above obtained values, and the Fe abundance, the LOS velocity dispersion and the redshift were allowed to vary. The fitting was done using a narrow energy range of $6.4\text{--}6.7 \text{ keV}$, excluding the energy band corresponding to the resonance line in the observer-frame ($6.575\text{--}6.6 \text{ keV}$). The obtained C-statistic/d.o.f. in the velocity fitting is $2822.38/2896$.

Table 4. Best-fitting bulk velocity (v_{bulk}) and LOS velocity dispersion (σ_v) values of with and without PSF correction.

Region	PSF corrected		PSF uncorrected	
	v_{bulk} (km s ⁻¹)	σ_v (km s ⁻¹)	v_{bulk} (km s ⁻¹)	σ_v (km s ⁻¹)
Reg 0	75 ⁺²⁶ ₋₂₈	189 ⁺¹⁹ ₋₁₈	43 ⁺¹² ₋₁₃	163 ⁺¹⁰ ₋₁₀
Reg 1	46 ⁺¹⁹ ₋₁₉	103 ⁺¹⁹ ₋₂₀	42 ⁺¹² ₋₁₂	131 ⁺¹¹ ₋₁₁
Reg 2	47 ⁺¹⁴ ₋₁₄	98 ⁺¹⁷ ₋₁₇	39 ⁺¹¹ ₋₁₁	126 ⁺¹² ₋₁₂
Reg 3	-39 ⁺¹⁵ ₋₁₆	106 ⁺²⁰ ₋₂₀	-19 ⁺¹¹ ₋₁₁	138 ⁺¹² ₋₁₂
Reg 4	-77 ⁺²⁹ ₋₂₈	218 ⁺²¹ ₋₂₁	-35 ⁺¹⁵ ₋₁₄	186 ⁺¹² ₋₁₂
Reg 5	-9 ⁺⁵⁵ ₋₅₆	117 ⁺⁶² ₋₇₃	-6 ⁺²⁵ ₋₂₆	125 ⁺²⁸ ₋₂₈
Reg 6	-45 ⁺²⁹ ₋₂₉	84 ⁺⁴⁴ ₋₅₄	-35 ⁺²² ₋₂₂	99 ⁺³¹ ₋₃₂

Figure 6 shows the obtained velocity maps with PSF correction. The corresponding velocity maps without PSF correction are shown in figure 7 for comparison. The best-fitting values are listed in table 4. The heliocentric correction of -26.4 km s^{-1} is applied in the bulk velocity maps.

When producing the PSF-corrected maps, the twelve spectra (Obs 3 and Obs 4 for Reg 0 to Reg 4 and Obs 1 for Reg 5 and Reg 6) were fitted simultaneously with all the cross-terms being incorporated through the matrix shown in table 3. The fitting procedure is complex and deconvolution is often unstable. We thus carefully examined the robustness of the results. These included the check of two parameter confidence surfaces based on C-statistics, i.e., redshift vs LOS velocity dispersion, Fe abundance vs redshift, and Fe abundance vs LOS velocity dispersion for each region, and LOS velocity dispersion vs LOS velocity dispersion and redshift vs redshift for each combination of regions. The redshift, LOS velocity dispersion, and Fe abundance are within 0.0165–0.0180, 0.0–250 km s⁻¹, and 0.35–0.85 solar, respectively. We found no strong correlations among parameters and also confirmed that the true minimum was found in the fitting.

In appendix 3, we also describe a different method of deriving the velocities that uses only the w line (which has been excluded in the fit above). It gives qualitatively similar results with the expected higher values of velocity dispersion. Further detailed investigations of the systematic uncertainties and various checks of the results are presented in appendices 2 and 3.

3.3 Limits on non-Gaussianity of line shapes

As shown in section 3.1, the observed widths of the Fe lines ($\sigma \sim 4 \text{ eV}$) are much broader than those expected by the convolution of the line spread function of the SXS (FWHM $\sim 5 \text{ eV}$ or $\sigma \sim 2 \text{ eV}$) with the thermal width ($\sigma_{\text{th}} \sim 2 \text{ eV}$ for Fe at $kT \sim 4 \text{ keV}$). Note also that uncertainties of instrumental energy scale and the line spread function at around 6 keV are smaller than the observed widths, as

Table 5. Centroid energy in the observer frame, width, significance, and goodness-of-fit of lines detected at $> 5\sigma$.

Line	Line information			Fitting information*			Note**
	Centroid energy [†] (eV)	σ_{v+th} (km s ⁻¹)	Significance [‡]	Energy band (keV)	C-statistic	d.o.f.	
Si Ly α	1969.32 \pm 0.21	224 ⁺⁴⁹ ₋₅₄	12.9	1.945–1.995	40.27	45	(1)
Si Ly β	2333.73 \pm 0.49	327 ⁺⁷¹ ₋₆₈	7.4	2.28–2.38	71.66	94	
S He α	2417.05 \pm 0.38	256 ⁺⁵⁹ ₋₅₇	8.1	2.355–2.45	73.47	90	
S Ly α	2575.83 \pm 0.11	192 ⁺²¹ ₋₂₂	27.2	2.53–2.62	117.17	85	
S Ly β	3052.33 \pm 0.26	198 ⁺³⁹ ₋₃₈	10.9	3.00–3.14	116.85	132	
Ar He α	3084.46 \pm 0.34	150 ⁺⁴⁷ ₋₅₀	8.5	3.00–3.14	99.95	132	
Ar Ly α	3265.12 \pm 0.27	260 ⁺³⁸ ₋₃₇	14.3	3.235–3.29	38.94	50	(2)
Ca He α	3835.26 \pm 0.19	186 ⁺²¹ ₋₂₀	15.8	3.77–3.855	55.85	79	
Ca Ly α	4036.97 \pm 0.35	202 ⁺³⁹ ₋₃₃	13.4	3.98–4.10 [§]	94.01	95	
Fe He α z	6522.97 \pm 0.11	166 \pm 5	44.3	6.47–6.63	167.79	148	
Fe He α w	6586.13 ^{+0.06} _{-0.07}	195 \pm 3	78.8	6.47–6.63	182.37	148	(3)
Fe Ly α	6854.49 \pm 0.24	183 \pm 11	18.1	6.77–6.89	143.74	113	
Ni He α	7671.73 ^{+0.60} _{-0.61}	224 ⁺³⁶ ₋₃₃	8.0	7.55–7.71	145.35	155	(4)
Fe He β	7744.83 ^{+0.22} _{-0.23}	178 ⁺¹¹ ₋₁₀	27.5	7.70–7.80	82.35	94	
Fe Ly β	8112.19 ^{+0.84} _{-0.46}	0 ⁺⁷⁵ ₋₀	5.9	8.05–8.22	152.86	162	(5)
Fe He γ	8152.44 \pm 0.50	189 \pm 20	12.5	8.05–8.22	146.75	162	(6)

* C-statistic and d.o.f. are those in the specified energy band.

[†] Energy of the most prominent component, unless specified otherwise.

[‡] Significance was determined by dividing the normalization by its 1σ error.

[§] Energy range from 4.07 keV to 4.09 keV was ignored, to exclude Ar Ly γ .

^{||} Gaussians were used for both z and w lines.

** (1) Line width changed from 1.85^{+0.41}_{-0.42} eV to 1.50^{+0.33}_{-0.36} eV, by adding Obs 2 data. The parameters may be unreliable. (2) Line width changed from 2.24^{+0.51}_{-0.52} eV to 2.88 \pm 0.42 eV, by adding Obs 2 data. The parameters may be unreliable. (3) This line is likely to be optically thick and affected by resonance scattering. (4) This energy range is contaminated by Fe satellite lines, and the parameters may be unreliable. (5) This energy range is contaminated by various satellite lines. In addition, the line width changed from 9.0^{+2.8}_{-2.6} eV to 0.0^{+2.1}_{-0.0} eV by adding Obs 2 data. The parameters may be unreliable. (6) This energy range is contaminated by various satellite lines. The parameters might be affected by them.

shown in appendix 2. They are instead governed by hydrodynamic motion of the gas. We thus aim to obtain further information on the gas velocity distribution by examining the line shapes in detail. In figures 2 and 3, fitting results of S Ly α , Fe He α , Ly α , and He β lines from Obs 3 and 4 are shown with residuals (ratios of the data to the best-fit model). In what follows, we make use of Obs 2 to improve the statistics and further investigate the line shapes.

The observed centroid energy of the Fe He α resonance line of Obs 2 is about 1.8 eV lower

Table 6. Best-fit widths when Voigt functions were used.

	Gaussian width (σ) (km s^{-1})	Lorentzian width (FWHM) (km s^{-1})	C-statistic	d.o.f.	Natural width (FWHM)* (km s^{-1})
Fe He α w	194 ± 3	$0.10^{+0.09}_{-0.03}$	182.04	147	13.9
Fe Ly α	113^{+14}_{-13}	172^{+29}_{-17}	137.44	112	8.2
Fe He β	137 ± 11	114^{+20}_{-19}	80.39	93	3.0

* Calculated using the Einstein A coefficient shown in AtomDB.

than that of Obs 3, and its width (σ) is about 0.36 eV broader, despite their similar pointing directions. Obs 2 (and Obs 1) occurred while the SXS dewar was still coming into thermal equilibrium after launch (Fujimoto et al. 2016), and these discrepancies come from the limitations of the method used to correct the drifting energy scale. The energy scale of the Obs 2 data was corrected as follows, to align their line centers. First, the centroid energy of each line of Obs 2 and 3 was determined by fitting the data separately. Then the energy (PI column) of each photon in the event file of Obs 2 was recalculated by multiplying a factor $E_{\text{Obs 3}}/E_{\text{Obs 2}}$, where $E_{\text{Obs 2}}$ and $E_{\text{Obs 3}}$ are the best-fit line center energies of Obs 2 and Obs 3, respectively. The event files of Obs 2, 3, and 4 were then merged and spectral files were generated. Note that the correction factor was determined for each line and hence, a spectral file was generated for each line separately. Note also that no additional gain alignment among the detector pixels was applied. The spectra were fitted in the same manner as described in section 3.1. Note that, for Fe He α , the resonance (w) line and the forbidden (z) line were manually excluded from the atomic database and substituted by external Gaussians, to determine the parameters of these lines. The fitting results are shown in table 5.

In this section, we focus on three brightest and less contaminated Fe transitions, He α , Ly α , and He β . They are from the single element and have a common thermal broadening. In addition, their energies are close enough that we can assume no significant difference in the detector line spread functions. Any astronomical velocity deviation components can cause common residuals of the line shapes in velocity space. Figure 8 shows the spectra of these lines in velocity space, after subtracting the best-fitting continuum model and the components other than the main line (He α w , Ly α_1 , and He β_1), where the line center energies were set at the origin of the velocity. As we are interested in deviations from Gaussianity, ratios of the data to the best-fit Gaussian models were also shown in figure 8. Ratios of Ly α_1 and He β_1 were co-added. Positive (ratio > 1) features are seen at around $\pm(400\text{--}500) \text{ km s}^{-1}$, while there is a negative (ratio < 1) feature at around $+300 \text{ km s}^{-1}$. However, they are not as broad as the detector line spread function (FWHM $\sim 230 \text{ km s}^{-1}$). Therefore, we do not conclude that these are cluster-related velocity structures.

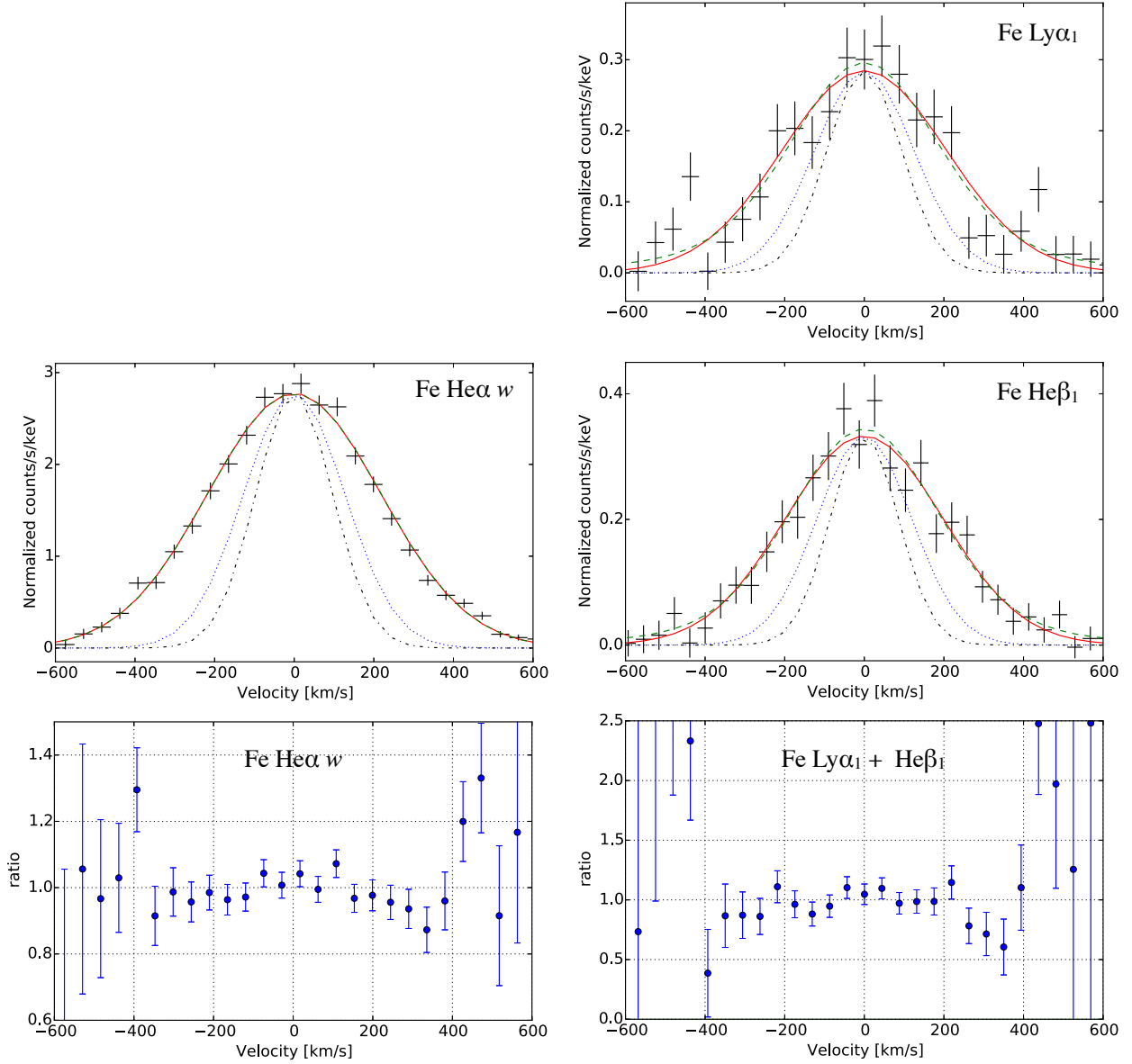


Fig. 8. (Upper panels) Data and best-fit models of Fe He α w , Ly α 1 , and He β 1 . The continuum model and the components other than the main line were subtracted. Solid (red) and dashed (green) lines represent the best-fit Gaussian and Voigtian profiles, respectively. Instrumental broadening with and without thermal broadening are indicated with dotted (blue) and dashed-dotted (black) lines. The horizontal axis is the velocity converted from the observed energy, where the line center is set at the origin. The bin size is 1 eV in the energy space, which corresponds to 45.5 km s $^{-1}$, 43.7 km s $^{-1}$, and 38.7 km s $^{-1}$, respectively. (Lower panels) The ratio spectra of the data to the best-fit Gaussian models, (left) for Fe He α w , and (right) for Fe Ly α 1 and He β 1 co-added. Note that the line spread function is not deconvolved from the data.

We also fitted each line in the same manner as described above, but using Voigt functions⁵ instead of Gaussians, for He α w , Ly α_1 , Ly α_2 , He β_1 , and He β_2 . The best-fitting shapes after subtracting the continuum and the components other than the main line are shown with dashed curves in the upper panels of figure 8, and the best-fit widths are summarized in table 6. The Lorentzian widths of Ly α and He β were much broader than the natural width. This may be due to large positive deviations at around $\pm(400\text{--}500)$ km s $^{-1}$. On the other hand, it was smaller than the natural width for He α . C-statistic decreased by 0.3, 6.3, and 2.0 for He α , Ly α and He β , respectively, when compared with that shown in table 5. Given these small improvements, we conclude that it is difficult to distinguish the Voigt and Gaussian line shapes using the present data.

After integrating the data of the entire SXS FOV ($60 \text{ kpc} \times 60 \text{ kpc}$), no clear deviations from Gaussianity were found. This may be because deviations are spatially averaged and smeared out. To investigate the line profile in smaller areas, we extracted spectra from several 2×2 pixel ($20 \times 20 \text{ kpc}$) regions, and analyzed the Fe He α w profiles similarly. We found no common residuals clearly seen in Obs 2, 3, and 4 when the spectra of the pixels that corresponded to the same or similar sky regions were compared. We also separated the data into two groups, the central region (including the AGN) and the outer region, but obtained similar results. Finally, as independent indicators, the skewness and the kurtosis of the line profiles were calculated, and they were broadly consistent with those of Gaussian. No clear deviation from Gaussianity was found.

3.4 Ion temperature measurements

In the analysis presented in previous sections, the observed line profiles are analyzed assuming that the ions are in thermal equilibrium with electrons and share the same temperature. High-resolution spectra by Hitomi provide us the first opportunity to directly test this assumption for galaxy clusters. As discussed in section 4, equilibration between electrons and ions takes longer than thermalization of the electron and ion distributions. A difference between the ion and electron temperatures may indicate a departure from thermal equilibrium.

The LOS velocity dispersion due to an isotropic thermal motion of ions is given by $\sigma_{\text{th}} = \sqrt{kT_{\text{ion}}/m_{\text{ion}}}$, where k is the Boltzmann constant, T_{ion} is the ion kinetic temperature, and m_{ion} is the ion mass. The LOS velocity dispersion from random hydrodynamic gas motions including turbulence, σ_{v} , is assumed common for all the elements. Since only the former depends on m_{ion} , one can in principle measure σ_{th} (i.e., T_{ion}) and σ_{v} separately by combining the widths of lines originating from

⁵ For the Voigt function fitting, we used the patched model that is the same code as implemented in XSPEC 12.9.11. See also <https://heasarc.gsfc.nasa.gov/xanadu/xspec/issues/issues.html>.

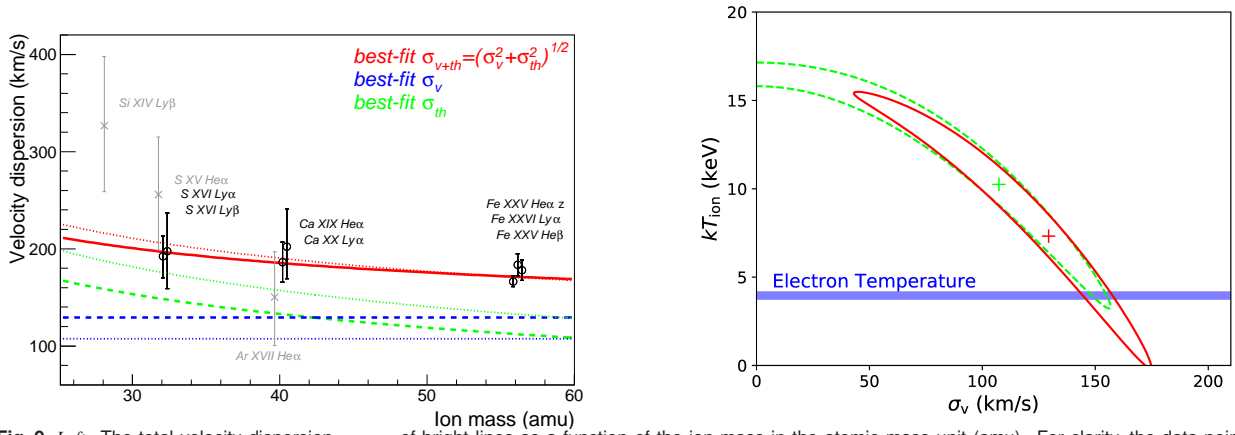


Fig. 9. *Left:* The total velocity dispersion σ_{v+th} of bright lines as a function of the ion mass in the atomic mass unit (amu). For clarity, the data points for the same element are slightly shifted horizontally. Black circles and gray crosses denote the lines detected at more than 10σ significance and at $5 - 10\sigma$ significance, respectively. Solid and dashed lines show the best-fit relation $\sigma_{v+th} = (\sigma_{th}^2 + \sigma_v^2)^{1/2}$ (red solid) and its components σ_{th} (green dashed) and σ_v (blue dashed) for the $> 10\sigma$ lines. Dotted lines are the best-fit relation σ_{v+th} (red dotted) and its components σ_{th} (green dotted) and σ_v (blue dotted) for the $> 5\sigma$ lines. *Right:* The 68% confidence regions of kT_{ion} and σ_v for two parameters of interest ($\Delta\chi^2 = 2.3$) with a plus marking the best-fit values. Red solid and green dashed contours represent the results for the $> 10\sigma$ and $> 5\sigma$ lines, respectively. For reference, the blue horizontal bar indicates the range of the electron temperature measured in T paper.

different heavy elements. For example, $kT_{ion} = 4$ keV corresponds to $\sigma_{th} = 83, 98, 110, 120$ km s⁻¹ for Fe, Ca, S, and Si, respectively. These thermal velocities tend to be smaller than σ_v even for the lightest of currently observed elements, making the measurement of T_{ion} challenging. In what follows, we assume that the ions share a single kinetic temperature for simplicity.

The left panel of figure 9 shows the total velocity dispersion σ_{v+th} of lines detected at more than 5σ significance listed in table 5. Unreliable measurements marked by notes 1–6 in table 5 have been excluded. The lines from different elements show nearly consistent velocity dispersions with a weakly-decreasing trend with ion mass. They are fit by $\sigma_{v+th} = (\sigma_v^2 + \sigma_{th}^2)^{1/2}$ varying T_{ion} and σ_v as free parameters. The best-fit values are $kT_{ion} = 10.2^{+5.0}_{-4.6}$ keV and $\sigma_v = 107^{+35}_{-58}$ km s⁻¹, with $\chi^2 = 7.104$ for 8 degrees of freedom. If only the most secure measurements at more than 10σ significance (black circles in the left panel of figure 9) are used, the best-fit values are $kT_{ion} = 7.3^{+5.3}_{-5.0}$ keV and $\sigma_v = 129^{+32}_{-45}$ km s⁻¹, with $\chi^2 = 2.640$ for 5 degrees of freedom. If we vary just a single parameter σ_v by setting $\sigma_{th} = 0$, we obtain $\sigma_v = 174.3^{+4.1}_{-4.2}$ km s⁻¹ with $\chi^2 = 12.20$ for 9 degrees of freedom from the $> 5\sigma$ lines, and $\sigma_v = 173.4 \pm 4.2$ km s⁻¹ with $\chi^2 = 4.848$ for 6 degrees of freedom from the $> 10\sigma$ lines.

The red solid and green dashed contours in the right panel of figure 9 show the 68% confidence regions of T_{ion} and σ_v for the $> 10\sigma$ lines and the $> 5\sigma$ lines, respectively. As expected, a negative correlation is found between T_{ion} and σ_v . Albeit with large errors, the inferred ion temperature is consistent within the 68% confidence level with the electron temperature reported in T paper. The

calibrated SXS FWHM has a systematic error of ~ 0.15 eV (see appendix 2), which does not alter the results of this subsection. The present errors are dominated by the uncertainties of the widths of the lines in the low energy (2–4 keV) band; higher significance data at lower energies and inclusion of lighter elements will be crucial for improving the measurement.

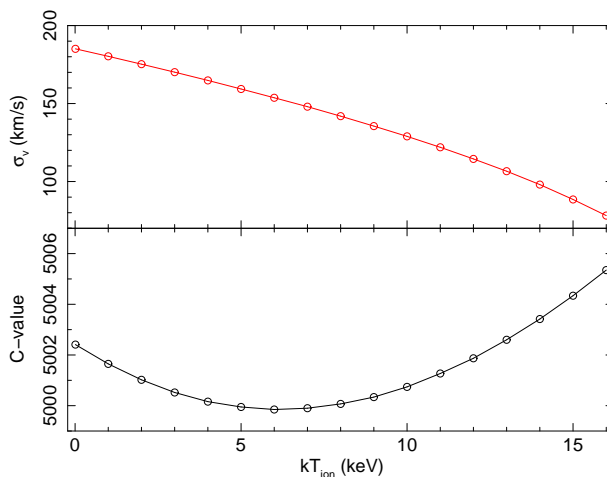


Fig. 10. Results of fitting the entire spectrum with a plasma code SPEX. Top and bottom panels show the optimal values of σ_v and C-statistic, respectively, for a given value of T_{ion} .

For comparison, we also infer the ion temperature by fitting the entire spectrum with a plasma code, SPEX v3.03.00 (Kaastra et al. 1996). Here we apply a gain correction using equation (A1) of Atomic paper to match the observed line energies to those implemented in SPEX. We fit the spectrum with models of the collisional ionization equilibrium plasma, the central AGN, and the NXB components. For the central AGN, we adopt the model parameters determined by AGN paper. We exclude the energy band covering the Fe XXV He α w line to eliminate the effect of resonance scattering. Figure 10 shows the optimal values of C-statistic and σ_v for a given value of T_{ion} . The best-fit values are $kT_{\text{ion}} = 6.0^{+4.2}_{-3.7}$ keV and $\sigma_v = 153^{+21}_{-27}$ km s $^{-1}$, with the C-statistic value of 4999.86 for 4653 degrees of freedom. Again a negative correlation between T_{ion} and σ_v is found. These results are consistent with those derived from a set of bright lines shown in figure 9.

Note that a similar analysis using SPEX is also performed in Atomic paper. They present the results when the Fe XXV He α w line is included in the fit. Since this line is likely subject to resonance scattering (RS paper), the fitted value of T_{ion} depends on how the radiative transfer effect is taken into account. They show that a simple absorption model implemented in SPEX yields the value of T_{ion} in good agreement with T_e (see section 7.1 of Atomic paper for details).

4 Discussion

4.1 The origin of gas motions

The Hitomi SXS observations provided the first direct measurements of the LOS velocities and velocity dispersions of the hot ICM in the core of the Perseus cluster. Using the optically thin emission lines, we find that the LOS velocity dispersion peaks toward the cluster center and around the prominent northwestern ‘ghost’ bubble, reaching $\sigma_v \sim 200 \text{ km s}^{-1}$. These velocity dispersion peaks are seen in both PSF-corrected and uncorrected maps. Outside of these peaks, the LOS velocity dispersion appears constant at $\sigma_v \sim 100 \text{ km s}^{-1}$. Note that the velocity dispersion peak at the center is seen in the maps derived by both methods, excluding and including the resonance w line (appendix 3). The peak toward the ghost bubble is not seen when the w line is used for the velocity fits (appendix 3), so its existence is less certain.

The maximum velocity of 100 km s^{-1} determined from line shifts within the investigated area indicates that the velocity of large scale flows is at least $v_{\text{bulk}} = 100 \text{ km s}^{-1}$. While some theoretical arguments predict a velocity offset of the order of $\sim 100 \text{ km s}^{-1}$ between the central galaxy and the ICM (Inoue 2014), the zero point of our observed bulk shear is consistent with the redshift of NCG 1275. We note that as the photons produced within the central $r \sim 100 \text{ kpc}$ climb up the gravitational potential well of the cluster, they are also affected by a gravitational redshift of $\sim 20 \text{ km s}^{-1}$. This shift should be considered in the absolute value of each redshift measurement. The v_{bulk} values are relative values between NGC 1275 and the ICM, and so the gravitational redshift is mostly canceled out. The relative gravitational redshift across the FOV is $\sim 5 \text{ km s}^{-1}$.

During the process of hierarchical structure formation, turbulent gas motions are driven on Mpc scales by mergers and accretion flows which convert their kinetic energy into turbulence (e.g. Brüggén & Vazza 2015). These turbulent motions then cascade down from the driving scales to dissipative scales, heating the plasma, (re-)accelerating cosmic-rays, and amplifying the magnetic fields (e.g. Brunetti & Lazarian 2007; Miniati & Beresnyak 2015). In the Perseus cluster, turbulence is also likely to contribute to powering the radio emission of the minihalo (Burns et al. 1992; Sijbring 1993; Walker et al. 2017) by re-accelerating the relativistic electrons originating from the AGN and/or hadronic interactions (e.g. Gitti et al. 2002; ZuHone et al. 2013).

Turbulence is also expected to be driven on smaller scales by the AGN, galaxy motions, gas sloshing, and hydrodynamic and magneto-thermal instabilities in the ICM (e.g. Churazov et al. 2002; Gu et al. 2013; Mendygral et al. 2012; Ichinohe et al. 2017; ZuHone et al. 2013, 2017). The low, relatively uniform velocity dispersion observed in the Perseus core is also consistent with that expected for turbulence induced in the cool core by sloshing (ZuHone et al. 2013). Several cold fronts are

seen in the Perseus X-ray images (Churazov et al. 2003; Simionescu et al. 2012; Walker et al. 2017), which reveal a sloshing core. If the observed velocity dispersion is indeed mostly sloshing induced, then an interesting prediction for future observations is that the observed dispersion will abruptly change across the cold fronts, which are mostly located outside the Hitomi FOV.

The observed peaks in σ_v appear to indicate that gas motions are driven both at the cluster center by the current AGN inflated bubbles and by the buoyantly rising ghost bubbles with diameters of ~ 25 kpc. The observed peaks in σ_v could be due to superposed streaming motions around the bubbles and turbulence. This observation appears to contradict models in which gas motions are sourced only at the center (during the initial stages of bubble inflation) or only by structure formation. These results may indicate that both the current AGN inflated bubbles in the cluster center and the buoyantly rising ghost bubbles are driving gas motions in the Perseus cluster.

Part of the observed large scale motions of $v_{\text{bulk}} \sim 100 \text{ km s}^{-1}$ might be due to streaming motions around and in the wakes of buoyantly rising bubbles as well. As already pointed out in H16, to the north of the core, the trend in the LOS velocities of the ICM is consistent with the trend in the velocities of the molecular gas within the northern optical emission line filaments (Salomé et al. 2011). These trends are consistent with the model where the optical emission line nebulae and the molecular gas result from thermally unstable cooling of low entropy gas uplifted by buoyantly rising bubbles (e.g. Hatch et al. 2006; McNamara et al. 2016).

However, most of the bulk motions are likely driven by the gas sloshing in the core of the Perseus cluster (Churazov et al. 2003; Walker et al. 2017; ZuHone et al. 2017). The gas sloshing observed in the innermost cluster core, $r \lesssim 100$ kpc, might be due to strong AGN outbursts (Churazov et al. 2003) or due to a disturbance of the cluster gravitational potential caused by a recent subcluster infall (e.g. Markevitch & Vikhlinin 2007) which is likely related to the large-scale sloshing in this system (Simionescu et al. 2012). The molecular gas can be advected by the sloshing hot gas, resulting in their similar LOS velocities. The shearing motions associated with gas sloshing are also expected to contribute to the velocity dispersion observed throughout the investigated area.

Given the large density gradient in the core of the Perseus cluster, the effective length along the LOS from which the largest fraction of line flux (and measured line width) arises, L_{eff} , is rapidly increasing as a function of radius. The increase of the effective length, L_{eff} , with growing projected distance r implies that larger and larger eddies contribute to the observed line broadening. Therefore, as shown by Zhuravleva et al. (2012), for Kolmogorov-like turbulence driven on scales larger than ~ 100 kpc, we would expect to see a radially increasing LOS velocity dispersion. For example, for turbulence driven on scales of 200 kpc, we would expect a factor of 1.7 increase in the measured velocity dispersion over the radial range of 100 kpc (from the core out to $r \sim 100$ kpc assuming the

density profile of the Perseus cluster). The lack of observed radial increase of σ_v might indicate that the turbulence in the core of the Perseus cluster is driven primarily on scales smaller than ~ 100 kpc. The relative uniformity of the dispersion is also consistent with sloshing-induced turbulence, which is mostly limited to the cool core in the absence of large-scale disturbances such as a major merger (see figures 14–16 in ZuHone et al. 2013).

While turbulence on spatial scales $L < L_{\text{eff}}$ will increase the observed line widths and the measured σ_v , gas motions on scales $L > L_{\text{eff}}$ will shift the line centroids. The superposition of large scale motions over the LOS within our extraction area should therefore lead to non-Gaussian features in the observed line shapes (e.g. Inogamov & Sunyaev 2003). The lack of evidence for non-Gaussian line shapes in the spectral lines extracted over a spatial scale of ~ 100 kpc (see section 3.3) indicates that the observed velocity dispersion is dominated by small scale motions and corroborates the conclusion that, in the core of the cluster, the driving scale of the turbulence is mostly smaller than ~ 100 kpc.

From a suite of cosmological cluster simulations by Nelson et al. (2014), and an isolated high-resolution cluster simulation with cooling and AGN feedback physics by Gaspari et al. (2012), Lau et al. (2017) generated a set of mock Hitomi SXS spectra to study the distribution and the characteristics of the observed velocities. They concluded that infall of subclusters and mechanical AGN feedback are the key complementary drivers of the observed gas motions. While the gentle, self-regulated mechanical AGN feedback sustains significant velocity dispersions in the inner innermost cool core, the large-scale velocity shear at $\gtrsim 50$ kpc is due to mergers with infalling groups. The comparison with their simulations also suggests that the AGN feedback is “gentle”, with many small outbursts instead of a few isolated powerful ones (see also Fabian et al. 2006; Fabian 2012; McNamara & Nulsen 2012; McNamara et al. 2016). Similar conclusions were reached in the simulations by Bourne & Sijacki (2017).

4.2 Kinetic pressure support

One of the key implications of the gas velocities measured in section 3 is that hydrostatic equilibrium holds to better than 10% near the center of the Perseus cluster. The results presented in figure 6 suggest that, if the observed velocity dispersion is due to isotropic turbulence, the inferred range of $\sigma_v \sim 100\text{--}200$ km s⁻¹ corresponds to 2–6% of the thermal pressure support of the gas with $kT = 4$ keV.

The large scale bulk motion will also contribute to the total kinetic energy. Assuming further that the observed line shifts are due to bulk motions with velocities of $v_{\text{bulk}} = 100$ km s⁻¹ with respect to the cluster center, the fraction of the kinetic to thermal energy density is

$$\frac{\epsilon_{\text{kin}}}{\epsilon_{\text{therm}}} = \frac{\mu m_{\text{p}}(3\sigma_{\text{v}}^2 + v_{\text{bulk}}^2)}{3kT} \sim 0.02 - 0.07, \quad (1)$$

for $kT = 4$ keV, where $\mu = 0.6$ is the mean molecular weight, and m_{p} is the proton mass. The expression can also be rewritten as $\epsilon_{\text{kin}}/\epsilon_{\text{therm}} = (\gamma/3)\mathcal{M}^2$, where the Mach number $\mathcal{M} = v_{\text{3D eff}}/c_{\text{s}} \sim 0.19 - 0.35$, $v_{\text{3D eff}} = \sqrt{3\sigma_{\text{v}}^2 + v_{\text{bulk}}^2}$ is the effective three dimensional velocity, $c_{\text{s}} = \sqrt{\gamma kT/\mu m_{\text{p}}} = 1030(kT/4 \text{ keV})^{1/2} \text{ km s}^{-1}$ is the sound speed, and $\gamma = 5/3$ is the adiabatic index. The small amount of the kinetic energy density supports the validity of total cluster mass measurements under the assumption of hydrostatic equilibrium (e.g., Allen et al. 2011), at least in the cores of galaxy clusters.

We note, however, that if the velocity dispersion is mostly sloshing induced, we might be underestimating the kinetic energy density. Sloshing in the Perseus cluster appears to be mostly in the plane of the sky and ZuHone et al. (2013) show that such a relative geometry results in a total kinetic energy being a factor $(5-6)\sigma_{\text{v}}^2$, compared to the factor of 3 in Equation 1 for isotropic motions. This would change the upper bound of the kinetic to thermal pressure ratio to 0.11–0.13.

4.3 Maintaining the balance between cooling and heating

The gas in the core of galaxy clusters appears to be in an approximate global thermal balance, which is likely maintained by several heating and energy transport mechanisms taking place simultaneously. One possible source of heat is the central AGN. Relativistic jets, produced by the central AGN drive weak shocks with Mach numbers of 1.2–1.5 (e.g. Forman et al. 2005, 2007, 2017; Nulsen et al. 2005; Simionescu et al. 2009a; Million et al. 2010; Randall et al. 2011, 2015) and inflate bubbles of relativistic plasma in the surrounding X-ray-emitting gas (e.g. Boehringer et al. 1993; Churazov et al. 2000; Fabian et al. 2003, 2006; Bîrzan et al. 2004; Dunn et al. 2005; Forman et al. 2005, 2007; Dunn & Fabian 2006, 2008; Rafferty et al. 2006; McNamara & Nulsen 2007). The bubbles appear to be inflated gently, with most of the energy injected by the AGN going into the enthalpy of bubbles and only $\lesssim 20\%$ carried by shocks (Forman et al. 2017; Zhuravleva et al. 2016; Tang & Churazov 2017). After detaching from the jets, the bubbles rise buoyantly and they often entrain and uplift large quantities of low entropy gas from the innermost regions of their host galaxies (Simionescu et al. 2008, 2009b; Kirkpatrick et al. 2009, 2011; Werner et al. 2010, 2011; McNamara et al. 2016). All of this activity is believed to take place in a tight feedback loop, where the hot ICM cools and accretes onto the central AGN, leading to the formation of jets which heat the surrounding gas, lowering the accretion rate, reducing the feedback, until the accretion eventually builds up again (for a review see McNamara & Nulsen 2007; Fabian 2012).

Many questions regarding the energy transport from the bubbles to the ICM remain. Part of the energy might be transported by turbulence generated in situ by bubble-driven gravity waves

oscillating within the gas (e.g. Churazov et al. 2001). While g-modes are efficient at spreading the energy azimuthally, they are not able to transport energy radially (e.g. Reynolds et al. 2015). Energy can also be carried by bubble-generated sound waves (Fabian et al. 2003; Fujita & Suzuki 2005; Sanders & Fabian 2007), which could propagate fast enough to heat the core (Fabian et al. 2017). The energy from bubbles can also be transported to the ICM by cosmic ray streaming and mixing (e.g. Loewenstein et al. 1991; Guo & Oh 2008; Fujita & Ohira 2011; Pfrommer 2013; Ruszkowski et al. 2017; Jacob & Pfrommer 2017) or by mixing of the bubbles (e.g. Hillel & Soker 2016, 2017).

The Hitomi SXS observation of the Perseus cluster allows us to explore the role of the dissipation of gas motions in keeping the ICM from cooling. As discussed in section 4.1, substantial part of the kinetic energy density in the core of the Perseus cluster could be generated by the AGN, which appears to produce a peak in σ_v toward the cluster center and possibly around the prominent northwestern ghost bubble. Heating by dissipation of turbulence, induced by buoyantly rising (at a significant fraction of the sound speed) AGN-inflated bubbles, provides an attractive regulating mechanism for balancing the cooling of the ICM through a feedback loop (e.g. McNamara & Nulsen 2007). The rising bubbles are expected to generate turbulence in their wakes and excite internal waves, which propagate efficiently in azimuthal directions and decay to volume-filling turbulence. Based on the analysis of surface brightness fluctuations measured with Chandra, Zhuravleva et al. (2014) showed that the heating rate from the dissipation of gas motions is capable of balancing the radiative cooling at each radius in the Perseus cluster. The direct measurements of the velocity dispersion by the Hitomi SXS are broadly consistent with these previous indirect deductions (see figure 11 in Zhuravleva et al. 2017, which compares the Chandra results with the earlier measurements reported by H16). Note, however, that the dissipation of observed gas motions is capable of balancing radiative cooling only if (i) these motions dissipate in less than 10% of the cooling timescale (\sim Gyr) and (ii) they are continuously replenished over the age of the Perseus cluster.

Numerical simulations by ZuHone et al. (2010) showed that gas sloshing can facilitate the heat inflow into the core from the outer, hotter cluster gas via mixing, which can be enough to offset radiative cooling in the bulk of the cool core, except the very center. While the dissipation of turbulence induced by mergers (Fujita et al. 2004) or galaxy motions (Balbus & Soker 1990; Gu et al. 2013) could also contribute to heating the ICM, they would be unable to maintain a fine-tuned feedback loop.

4.4 Thermal equilibrium between electrons and ions

We performed the first measurement of the ICM ion temperature, based on the thermal broadening of the emission lines. We find the ion temperature to be consistent with the electron temperature, albeit with large uncertainties. Equilibration via Coulomb collisions between the ions and electrons takes place over the timescale given by

$$t_{\text{eq}} \sim 6 \times 10^6 \text{ yr} \left(\frac{n_e}{10^{-2} \text{ cm}^{-3}} \right)^{-1} \left(\frac{kT}{4 \text{ keV}} \right)^{3/2}, \quad (2)$$

where n_e is the number density of electrons (Spitzer 1965; Zeldovich & Raizer 1966). The equilibration time scales for electrons and for the ions are much shorter by factors of about $m_p/m_e \simeq 1800$ and $\sqrt{m_p/m_e} \simeq 43$, respectively, where m_p is the proton mass and m_e is the electron mass. Because the ions in the ICM are almost fully ionised and the rate of Coulomb collisions is proportional to the electric charge squared, their equilibration time scale is governed by that of protons; the ions equilibrate with protons faster than protons among themselves. Therefore, if the ICM has equilibrated via Coulomb collisions, equation (2) gives a lower limit to the time elapsed since the last major heat injection. This timescale is much shorter than any relevant merger or AGN-related timescales, thus we did not expect to find a discrepancy between T_e and T_{ion} .

5 Conclusions

In this paper, we have presented Hitomi observations of the atmospheric gas motions in the core, $r \lesssim 100$ kpc, of the Perseus galaxy cluster. Our findings are summarized as follows.

1. We have resolved and measured the line widths of He-like and H-like ions of Si, S, Ar, Ca, and Fe in the hot ICM for the first time.
2. Using the optically thin emission lines and after correcting for the point spread function of the telescope, we find that the line-of-sight velocity dispersion of the hot gas is mostly low and uniform. The line-of-sight velocity dispersion of the hot gas reaches maxima of approximately 200 km s^{-1} toward the central AGN and toward the AGN inflated north-western ‘ghost’ bubble. Elsewhere within the observed region, the velocity dispersion appears nearly uniform at $\sigma_v \sim 100 \text{ km s}^{-1}$. The systematic uncertainty affecting the best-fit line-of-sight velocity dispersion values is $\lesssim 20 \text{ km s}^{-1}$ (gain), $\lesssim 3 \text{ km s}^{-1}$ (line spread function) and $\lesssim 5 \text{ km s}^{-1}$ (PSF shape) in most cases.
3. We detect a large scale bulk velocity gradient with an amplitude of $\sim 100 \text{ km s}^{-1}$ across the cluster center, consistent with sloshing induced motions.
4. The mean redshift of the hot atmosphere is consistent with that of the stars of the central galaxy NGC 1275.

5. The shapes of well-resolved optically thin emission lines are consistent with Gaussian. The lack of evidence for non-Gaussian line shapes indicates that the observed velocity dispersion is dominated by small scale motions. Our results imply that the driving scale of turbulence is mostly smaller than ~ 100 kpc.
6. If the observed gas motions are isotropic, the kinetic pressure support in the cluster core is smaller than 10% of the thermal pressure.
7. Combining the widths of the lines formed from various elements, we have obtained the first direct constraints on the thermal motions of the ions in the hot ICM. We find no evidence of deviation between the ion temperature and the electron temperature.

Owing to the short lifetime of Hitomi, our results are restricted to the central region of a single galaxy cluster. Future X-ray calorimeter missions, e.g., the X-ray Astronomy Recovery Mission (XARM) and Athena (Nandra et al. 2013), will be crucial for extending the measurements to larger radii and a larger number of clusters, thereby providing further insights into the dynamics of galaxy clusters.

Author Contributions

Y. Ichinohe and S. Ueda led this study and wrote the final manuscript along with T. Kitayama, B. McNamara, N. Werner, R. Fujimoto, S. Inoue, M. Markevitch, and C. Kilbourne. Y. Ichinohe and S. Ueda performed the analysis of section 3.2 and appendices 2, 3.1, 3.2, and 3.4. R. Fujimoto and K. Tanaka conducted the analysis of sections 3.1 and 3.3. S. Inoue and T. Kitayama performed the analysis of section 3.4. N. Werner, B. McNamara, and I. Zhuravleva provided various inputs to section 4. R. Canning measured the new redshift of the central galaxy NGC 1275 presented in appendix 1. M. Markevitch performed the analysis of appendix 3.3. Q. Wang contributed to the analysis of appendix 3.1. T. Tamura, N. Ota, M. Tsujimoto, K. Sato, and S. Nakashima contributed to the velocity mapping analysis and studies on systematic uncertainties. R. Fujimoto, C. Kilbourne, and S. Porter achieved the development, integration tests, and in-orbit operation of the SXS. Y. Maeda supported the evaluation of the PSF scattering effect. T. Hayashi, S. Kitamoto, and I. Zhuravleva evaluated the impact of the gravitational redshift. The science goals of Hitomi were discussed and developed over more than 10 years by the ASTRO-H Science Working Group (SWG), all members of which are authors of this manuscript. All the instruments were prepared by joint efforts of the team. The manuscript was subject to an internal collaboration-wide review process. All authors reviewed and approved the final version of the manuscript.

Acknowledgments

We are grateful to the anonymous referee for helpful suggestions and comments. We acknowledge Yuya Kinoshita for his detailed analysis on the non-Gaussianity in 2x2 pixel scale and evaluation of skewness and kurtosis, Yu Kai, Ayumi Tsuji, and Tomohiro Nakano for supporting data analysis. We thank the support from the JSPS Core-to-Core Program. We acknowledge all the JAXA members who have contributed to the ASTRO-H (Hitomi) project. All U.S. members gratefully acknowledge support through the NASA Science Mission Directorate. Stanford and SLAC members acknowledge support via DoE contract to SLAC National Accelerator Laboratory DE-AC3-76SF00515. Part of this work was performed under the auspices of the U.S. DoE by LLNL under Contract DE-AC52-07NA27344. Support from the European Space Agency is gratefully acknowledged. French members acknowledge support from CNES, the Centre National d'Études Spatiales. SRON is supported by NWO, the Netherlands Organization for Scientific Research. Swiss team acknowledges support of the Swiss Secretariat for Education, Research and Innovation (SERI). The Canadian Space Agency is acknowledged for the support of Canadian members. We acknowledge support from JSPS/MEXT KAKENHI grant numbers 15J02737, 15H00773, 15H00785, 15H02090, 15H03639, 15H05438, 15K05107, 15K17610, 15K17657, 16J00548, 16J02333, 16H00949, 16H06342, 16K05295, 16K05296, 16K05300, 16K13787, 16K17672, 16K17673, 17J07948, 21659292, 23340055, 23340071, 23540280, 24105007, 24244014, 24540232, 25105516, 25109004, 25247028, 25287042, 25400236, 25800119, 26109506, 26220703, 26400228, 26610047, 26800102, JP15H02070, JP15H03641, JP15H03642, JP15H06896, JP16H03983, JP15J01845, JP16K05296, JP16K05309, JP16K17667, and JP16K05296. The following NASA grants are acknowledged: NNX15AC76G, NNX15AE16G, NNX15AK71G, NNX15AU54G, NNX15AW94G, and NNG15PP48P to Eureka Scientific. H. Akamatsu acknowledges support of NWO via Veni grant. C. Done acknowledges STFC funding under grant ST/L00075X/1. A. Fabian and C. Pinto acknowledge ERC Advanced Grant 340442. P. Gandhi acknowledges JAXA International Top Young Fellowship and UK Science and Technology Funding Council (STFC) grant ST/J003697/2. Y. Ichinohe, K. Nobukawa, H. Seta, S. Inoue, and T. Hayashi are supported by the Research Fellow of JSPS for Young Scientists. N. Kawai is supported by the Grant-in-Aid for Scientific Research on Innovative Areas "New Developments in Astrophysics Through Multi-Messenger Observations of Gravitational Wave Sources". S. Kitamoto is partially supported by the MEXT Supported Program for the Strategic Research Foundation at Private Universities, 2014-2018. B. McNamara and S. Safi-Harb acknowledge support from NSERC. T. Dotani, T. Takahashi, T. Tamagawa, M. Tsujimoto and Y. Uchiyama acknowledge support from the Grant-in-Aid for Scientific Research on Innovative Areas "Nuclear Matter in Neutron Stars Investigated by Experiments and Astronomical Observations". Q. Wang was supported by Chandra grants GO3-14144Z, GO5-16147Z and AR5-16013X. N. Werner is supported by the Lendület LP2016-11 grant from the Hungarian Academy of Sciences. D. Wilkins is supported by NASA through Einstein Fellowship grant number PF6-170160, awarded by the Chandra X-ray Center, operated by the Smithsonian Astrophysical Observatory for NASA under contract NAS8-03060.

We thank contributions by many companies, including in particular, NEC, Mitsubishi Heavy Industries, Sumitomo Heavy Industries, and Japan Aviation Electronics Industry. We acknowledge Google Inc. for their web-based services which really boosted our productivity. Finally, we acknowledge strong support from the following engineers. JAXA/ISAS: Chris Baluta, Nobutaka Bando, Atsushi Harayama, Kazuyuki Hirose, Kosei Ishimura, Naoko Iwata, Taro Kawano, Shigeo Kawasaki, Kenji Minesugi, Chikara Natsukari, Hiroyuki Ogawa, Mina Ogawa, Masayuki Ohta, Tsuyoshi Okazaki, Shin-ichiro Sakai, Yasuko Shibano, Maki Shida, Takanobu Shimada, Atsushi Wada, Takahiro Yamada; JAXA/TKSC: Atsushi Okamoto, Yoichi Sato, Keisuke Shinozaki, Hiroyuki Sugita; Chubu U: Yoshiharu Namba; Ehime U: Keiji Ogi; Kochi U of Technology: Tatsuro Kosaka; Miyazaki U: Yusuke Nishioka; Nagoya U: Housei Nagano; NASA/GSFC: Thomas Bialas, Kevin Boyce, Edgar Canavan, Michael DiPirro, Mark Kimball, Candace Masters, Daniel Mcguinness, Joseph Miko, Theodore Muench, James Pontius, Peter Shirron, Cynthia Simmons, Gary Sneiderman, Tomomi Watanabe; ADNET Systems: Michael Witthoef, Kristin Rutkowski, Robert S. Hill, Joseph Eggen; Wyle Information Systems: Andrew Sargent, Michael Dutka; Noqsi Aerospace Ltd: John Doty; Stanford U/KIPAC: Makoto Asai, Kirk Gilmore; ESA (Netherlands): Chris Jewell; SRON: Daniel Haas, Martin Frericks, Philippe Laubert, Paul Lowes; U of Geneva: Philipp Azzarello; CSA: Alex Koujelev, Franco Moroso.

References

- Aharonian, F. A., Akamatsu, H., Akimoto, F., et al. 2017, *ApJL*, 837, L15
- Allen, S. W., Evrard, A. E., & Mantz, A. B. 2011, *ARA&A*, 49, 409
- Angelini, L., Terada, Y., Loewenstein, M., et al. 2016, in *Proc. SPIE*, Vol. 9905, Society of Photo-Optical Instrumentation Engineers (SPIE) Conference Series, 990514
- Arnaud, K. A. 1996, in *Astronomical Society of the Pacific Conference Series*, Vol. 101, *Astronomical Data Analysis Software and Systems V*, ed. G. H. Jacoby & J. Barnes, 17
- Bîrzan, L., Rafferty, D. A., McNamara, B. R., Wise, M. W., & Nulsen, P. E. J. 2004, *ApJ*, 607, 800
- Balbus, S. A., & Soker, N. 1990, *ApJ*, 357, 353
- Beiersdorfer, P., Phillips, T., Jacobs, V. L., et al. 1993, *ApJ*, 409, 846
- Blanton, E. L., Randall, S. W., Clarke, T. E., et al. 2011, *ApJ*, 737, 99
- Boehringer, H., Voges, W., Fabian, A. C., Edge, A. C., & Neumann, D. M. 1993, *MNRAS*, 264, L25
- Bourne, M. A., & Sijacki, D. 2017, *ArXiv e-prints*, arXiv:1705.07900
- Brüggen, M., & Vazza, F. 2015, in *Astrophysics and Space Science Library*, Vol. 407, *Magnetic Fields in Diffuse Media*, ed. A. Lazarian, E. M. de Gouveia Dal Pino, & C. Melioli, 599
- Brunetti, G., & Lazarian, A. 2007, *MNRAS*, 378, 245
- Bulbul, G. E., Smith, R. K., Foster, A., et al. 2012, *ApJ*, 747, 32
- Burns, J. O. 1990, *AJ*, 99, 14
- Burns, J. O., Sulkanen, M. E., Gisler, G. R., & Perley, R. A. 1992, *ApJL*, 388, L49
- Cappellari, M. 2017, *MNRAS*, 466, 798
- Cappellari, M., & Emsellem, E. 2004, *PASP*, 116, 138
- Carilli, C. L., Perley, R. A., & Harris, D. E. 1994, *MNRAS*, 270, 173
- Churazov, E., Brüggen, M., Kaiser, C. R., Böhringer, H., & Forman, W. 2001, *ApJ*, 554, 261
- Churazov, E., Forman, W., Jones, C., & Böhringer, H. 2000, *A&A*, 356, 788
- . 2003, *ApJ*, 590, 225
- Churazov, E., Sunyaev, R., Forman, W., & Böhringer, H. 2002, *MNRAS*, 332, 729
- Clarke, T. E., Blanton, E. L., & Sarazin, C. L. 2004, *ApJ*, 616, 178
- Conselice, C. J., Gallagher, III, J. S., & Wyse, R. F. G. 2001, *AJ*, 122, 2281
- den Herder, J. W., Brinkman, A. C., Kahn, S. M., et al. 2001, *A&A*, 365, L7
- Dunn, R. J. H., & Fabian, A. C. 2006, *MNRAS*, 373, 959
- . 2008, *MNRAS*, 385, 757
- Dunn, R. J. H., Fabian, A. C., & Taylor, G. B. 2005, *MNRAS*, 364, 1343
- Dupke, R. A., & Bregman, J. N. 2006, *ApJ*, 639, 781
- Dupke, R. A., Mirabal, N., Bregman, J. N., & Evrard, A. E. 2007, *ApJ*, 668, 781

Eckart, M., Porter, F. S., & Fujimoto, R. 2017, PASJ

Eckart, M. E., Adams, J. S., Boyce, K. R., et al. 2016, in Proc. SPIE, Vol. 9905, Society of Photo-Optical Instrumentation Engineers (SPIE) Conference Series, 99053W

Fabian, A. C. 2012, ARA&A, 50, 455

Fabian, A. C., Sanders, J. S., Allen, S. W., et al. 2003, MNRAS, 344, L43

Fabian, A. C., Sanders, J. S., Taylor, G. B., et al. 2006, MNRAS, 366, 417

Fabian, A. C., Walker, S. A., Russell, H. R., et al. 2017, MNRAS, 464, L1

Fabian, A. C., Sanders, J. S., Ettori, S., et al. 2000, MNRAS, 318, L65

Fabian, A. C., Sanders, J. S., Allen, S. W., et al. 2011, MNRAS, 418, 2154

Forman, W., Churazov, E., Jones, C., et al. 2017, [arXiv: 1705.01104], arXiv:1705.01104

Forman, W., Nulsen, P., Heinz, S., et al. 2005, ApJ, 635, 894

Forman, W., Jones, C., Churazov, E., et al. 2007, ApJ, 665, 1057

Foster, A. R., Ji, L., Smith, R. K., & Brickhouse, N. S. 2012, ApJ, 756, 128

Fujimoto, R., Takei, Y., Mitsuda, K., et al. 2016, in Proc. SPIE, Vol. 9905, Society of Photo-Optical Instrumentation Engineers (SPIE) Conference Series, 99053S

Fujita, Y., Matsumoto, T., & Wada, K. 2004, ApJL, 612, L9

Fujita, Y., & Ohira, Y. 2011, ApJ, 738, 182

Fujita, Y., & Suzuki, T. K. 2005, ApJL, 630, L1

Fujita, Y., Hayashida, K., Nagai, M., et al. 2008, PASJ, 60, 1133

Gabriel, A. H. 1972, MNRAS, 160, 99

Gaspari, M., Brighenti, F., & Temi, P. 2012, MNRAS, 424, 190

Gitti, M., Brunetti, G., & Setti, G. 2002, A&A, 386, 456

Gu, L., Gandhi, P., Inada, N., et al. 2013, ApJ, 767, 157

Guo, F., & Oh, S. P. 2008, MNRAS, 384, 251

Hatch, N. A., Crawford, C. S., Johnstone, R. M., & Fabian, A. C. 2006, MNRAS, 367, 433

Hillel, S., & Soker, N. 2016, MNRAS, 455, 2139

—. 2017, MNRAS, 466, L39

Hitomi Collaboration. 2017a, PASJ

—. 2017b, PASJ

—. 2017c, PASJ

—. 2017d, PASJ

Hitomi Collaboration, Aharonian, F., Akamatsu, H., et al. 2016, Nature, 535, 117

Ichinohe, Y., Simionescu, A., Werner, N., & Takahashi, T. 2017, MNRAS, 467, 3662

Inogamov, N. A., & Sunyaev, R. A. 2003, Astronomy Letters, 29, 791

Inoue, H. 2014, PASJ, 66, 60

Jacob, S., & Pfrommer, C. 2017, MNRAS, 467, 1478

Kaastra, J. S., Mewe, R., & Nieuwenhuijzen, H. 1996, in *UV and X-ray Spectroscopy of Astrophysical and Laboratory Plasmas*, ed. K. Yamashita & T. Watanabe, 411–414

Kalberla, P. M. W., Burton, W. B., Hartmann, D., et al. 2005, A&A, 440, 775

Kelley, R. L., Akamatsu, H., Azzarello, P., et al. 2016, in *Proc. SPIE, Vol. 9905, Society of Photo-Optical Instrumentation Engineers (SPIE) Conference Series, 99050V*

Kilbourne, C. A., Adams, J. S., Brekosky, R. P., et al. 2016, in *Proc. SPIE, Vol. 9905, Society of Photo-Optical Instrumentation Engineers (SPIE) Conference Series, 99053L*

Kirkpatrick, C. C., Gitti, M., Cavagnolo, K. W., et al. 2009, ApJL, 707, L69

Kirkpatrick, C. C., McNamara, B. R., & Cavagnolo, K. W. 2011, ApJL, 731, L23

Kitayama, T., Bautz, M., Markevitch, M., et al. 2014, ArXiv e-prints, arXiv:1412.1176

Lau, E. T., Gaspari, M., Nagai, D., & Coppi, P. 2017, ArXiv e-prints, arXiv:1705.06280

Leutenegger, M. A., Audard, M., Boyce, K. R., et al. 2016, in *Proc. SPIE, Vol. 9905, Society of Photo-Optical Instrumentation Engineers (SPIE) Conference Series, 99053U*

Liu, A., Yu, H., Tozzi, P., & Zhu, Z.-H. 2016, ApJ, 821, 29

Lodders, K., & Palme, H. 2009, *Meteoritics and Planetary Science Supplement*, 72, 5154

Loewenstein, M., Zweibel, E. G., & Begelman, M. C. 1991, ApJ, 377, 392

Maeda, Y., Sato, T., Hayashi, T., et al. 2017, PASJ

Markevitch, M. 1996, ApJL, 465, L1

Markevitch, M., Mushotzky, R., Inoue, H., et al. 1996, ApJ, 456, 437

Markevitch, M., & Vikhlinin, A. 2007, *Phys. Rep.*, 443, 1

Markevitch, M., Vikhlinin, A., & Mazzotta, P. 2001, ApJL, 562, L153

McNamara, B. R., & Nulsen, P. E. J. 2007, ARA&A, 45, 117

—. 2012, *New Journal of Physics*, 14, 055023

McNamara, B. R., O’Connell, R. W., & Sarazin, C. L. 1996, AJ, 112, 91

McNamara, B. R., Russell, H. R., Nulsen, P. E. J., et al. 2016, ApJ, 830, 79

McNamara, B. R., Wise, M., Nulsen, P. E. J., et al. 2000, ApJL, 534, L135

Mendygral, P. J., Jones, T. W., & Dolag, K. 2012, ApJ, 750, 166

Million, E. T., Werner, N., Simionescu, A., et al. 2010, MNRAS, 407, 2046

Miniati, F., & Beresnyak, A. 2015, *Nature*, 523, 59

Nandra, K., Barret, D., Barcons, X., et al. 2013, ArXiv e-prints, arXiv:1306.2307

Nelson, K., Lau, E. T., & Nagai, D. 2014, ApJ, 792, 25

Nishino, S., Fukazawa, Y., & Hayashi, K. 2012, PASJ, 64, 16

Nulsen, P. E. J., McNamara, B. R., Wise, M. W., & David, L. P. 2005, *ApJ*, 628, 629

Okajima, T., & Tsujimoto, M. 2017, *PASJ*

Okajima, T., Soong, Y., Serlemitsos, P., et al. 2016, in *Proc. SPIE*, Vol. 9905, Society of Photo-Optical Instrumentation Engineers (SPIE) Conference Series, 99050Z

Ota, N., & Yoshida, H. 2016, *PASJ*, 68, S19

Ota, N., Fukazawa, Y., Fabian, A. C., et al. 2007, *PASJ*, 59, 351

Pfrommer, C. 2013, *ApJ*, 779, 10

Pinto, C., Sanders, J. S., Werner, N., et al. 2015, *A&A*, 575, A38

Porter, F. S., Boyce, K. R., Chiao, M. P., et al. 2016, in *Proc. SPIE*, Vol. 9905, Society of Photo-Optical Instrumentation Engineers (SPIE) Conference Series, 99050W

Rafferty, D. A., McNamara, B. R., Nulsen, P. E. J., & Wise, M. W. 2006, *ApJ*, 652, 216

Randall, S. W., Forman, W. R., Giacintucci, S., et al. 2011, *ApJ*, 726, 86

Randall, S. W., Nulsen, P. E. J., Jones, C., et al. 2015, *ApJ*, 805, 112

Reynolds, C. S., Balbus, S. A., & Schekochihin, A. A. 2015, *ApJ*, 815, 41

Ruszkowski, M., Yang, H.-Y. K., & Reynolds, C. S. 2017, [arXiv:1701.07441], arXiv:1701.07441

Salomé, P., Combes, F., Revaz, Y., et al. 2011, *A&A*, 531, A85

Sanders, J. S., & Fabian, A. C. 2007, *MNRAS*, 381, 1381

—. 2013, *MNRAS*, 429, 2727

Sanders, J. S., Fabian, A. C., & Smith, R. K. 2011, *MNRAS*, 410, 1797

Sanders, J. S., Fabian, A. C., Smith, R. K., & Peterson, J. R. 2010, *MNRAS*, 402, L11

Sato, K., Matsushita, K., Ishisaki, Y., et al. 2008, *PASJ*, 60, S333

Sato, T., Matsushita, K., Ota, N., et al. 2011, *PASJ*, 63, S991

Sijbring, L. G. 1993, A radio continuum and HI line study of the perseus cluster

Simionescu, A., Roediger, E., Nulsen, P. E. J., et al. 2009a, *A&A*, 495, 721

Simionescu, A., Werner, N., Böhringer, H., et al. 2009b, *A&A*, 493, 409

Simionescu, A., Werner, N., Finoguenov, A., Böhringer, H., & Brüggén, M. 2008, *A&A*, 482, 97

Simionescu, A., Werner, N., Urban, O., et al. 2012, *ApJ*, 757, 182

Smith, R. K., Brickhouse, N. S., Liedahl, D. A., & Raymond, J. C. 2001, *ApJL*, 556, L91

Spitzer, L. 1965, *Physics of fully ionized gases*

Sugawara, C., Takizawa, M., & Nakazawa, K. 2009, *PASJ*, 61, 1293

Sun, M. 2009, *ApJ*, 704, 1586

Takahashi, T., Kokubun, M., Mitsuda, K., & et al. 2016, in *Proc. SPIE*, Vol. 9905, Society of Photo-Optical Instrumentation Engineers (SPIE) Conference Series, 99050U

Tamura, T., Hayashida, K., Ueda, S., & Nagai, M. 2011, *PASJ*, 63, S1009

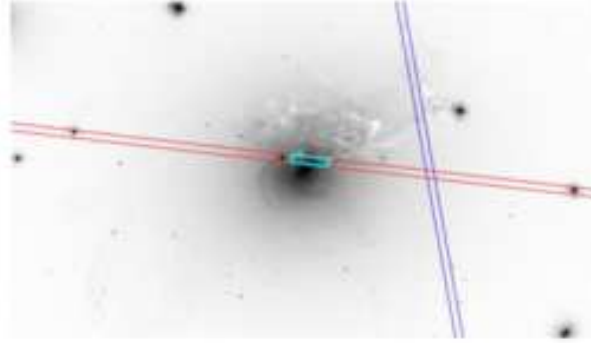


Fig. 11. The slit placement on NGC 1275. Our spectral extraction region is indicated with the cyan box on the red slit. Only the brighter parts of the low velocity system are extracted to avoid contamination by both a bright star and the high velocity system.

Tamura, T., Yamasaki, N. Y., Iizuka, R., et al. 2014, *ApJ*, 782, 38

Tang, X., & Churazov, E. 2017, *MNRAS*, 468, 3516

Ueda, S., Kitayama, T., & Dotani, T. 2017, *ApJ*, 837, 34

Walker, S. A., Hlavacek-Larrondo, J., Gendron-Marsolais, M., et al. 2017, *MNRAS*, 468, 2506

Wang, Q. H. S., Markevitch, M., & Giacintucci, S. 2016, *ApJ*, 833, 99

Werner, N., Simionescu, A., Million, E. T., et al. 2010, *MNRAS*, 407, 2063

Werner, N., Sun, M., Bagchi, J., et al. 2011, *MNRAS*, 415, 3369

Willingale, R., Starling, R. L. C., Beardmore, A. P., Tanvir, N. R., & O'Brien, P. T. 2013, *MNRAS*, 431, 394

Zeldovich, Y. B., & Raizer, Y. P. 1966, *Elements of gasdynamics and the classical theory of shock waves*

Zhuravleva, I., Allen, S. W., Mantz, A. B., & Werner, N. 2017, *ArXiv e-prints*, arXiv:1707.02304

Zhuravleva, I., Churazov, E., Kravtsov, A., & Sunyaev, R. 2012, *MNRAS*, 422, 2712

Zhuravleva, I., Churazov, E., Schekochihin, A. A., et al. 2014, *Nature*, 515, 85

Zhuravleva, I., Churazov, E., Arévalo, P., et al. 2016, *MNRAS*, 458, 2902

ZuHone, J., Miller, E. D., Bulbul, E., & Zhuravleva, I. 2017, *ArXiv e-prints*, arXiv:1708.07206

ZuHone, J. A., Markevitch, M., Brunetti, G., & Giacintucci, S. 2013, *ApJ*, 762, 78

ZuHone, J. A., Markevitch, M., & Johnson, R. E. 2010, *ApJ*, 717, 908

Appendix 1 New redshift measurement of NGC 1275 using absorption lines

Long slit spectroscopy was performed using the Intermediate dispersion Spectrograph and Imaging System (ISIS) at the 4.2 m William Herschel Telescope on the island of La Palma on 2007 December 29. The data were reduced using tailored IDL routines (adapted from the KRISIS IDL scripts by J.R. Mullaney 2008) for standard bias, flat field correction and wavelength calibration. The spectra

were then traced and extracted separately on each frame using Gaussian and Lorentz profile fits in the cross-dispersion direction. Only the brighter parts of the low velocity system are extracted to avoid contamination by both a bright star which is in the slit and the high velocity system (see figure 11). The spectra are median-combined. The wavelength calibration was checked and refined using bright sky Hg lines at air wavelengths of 4046.565Å and 4358.335Å. These features, especially at 4358Å, are strong in our spectra and allow a finer, more precise wavelength calibration.

We fit the median combined R300B arm spectra using pPXF, which is an IDL program to extract the stellar kinematics or stellar population from absorption-line spectra of galaxies using the Penalized Pixel-Fitting method (pPXF; Cappellari & Emsellem 2004; Cappellari 2017). We fit Miles stellar population synthesis models with an IMF slope of 1.3 and metallicity values ranging from -2.32 to $+0.22$. The stellar kinematics is fit with the emission lines masked out. We obtain a best fit redshift of $z = 0.017284 \pm 0.000039$ with only the statistical fitting uncertainties included. Including the upper and lower limits on wavelength calibration, we obtain $z = 0.017284 \pm 0.00005$. For comparison, fitting the [O II] emission line doublet in the same region as the absorption lines gives $z = 0.01697 \pm 0.00003$.

Appendix 2 Systematic uncertainty

A.2.1 Gain uncertainty

We achieved the systematic gain difference between Obs 3 and Obs 4 of $\lesssim 0.3$ eV at 6.586 keV (the line centroid of Fe He α w in observer frame) with the standard pipeline gain correction processes alone. As the pointings of Obs 1 and Obs 2 were performed before the temperature of the helium tank reached near thermal equilibrium, an additional energy scale adjustment (sxspersesus⁶), in addition to the standard pipeline gain correction, was applied to these datasets. As the FOV of Obs 2 overlaps with those of Obs 3 or Obs 4, we are able to compare the gain among these observations directly. After the gain adjustment, the data of Obs 2 have a gain offset of ~ 2 eV at 6.586 keV, compared to Obs 3 (and Obs 4). As the FOV of Obs 1 does not overlap with those of Obs 2, 3 or 4, the absolute gain scale of Obs 1 is difficult to estimate. Considering the ~ 2 eV gain offset of Obs 2, we think that the systematic uncertainty of the energy scale of Obs 1, is at least ~ 2 eV relative to Obs 3. The pixel-to-pixel relative gain uncertainty within each single pointing is ~ 0.5 eV. More details are described in Eckart et al. (2017).

⁶ <https://heasarc.gsfc.nasa.gov/docs/hitomi/analysis/ahhelp/sxspersesus.html>

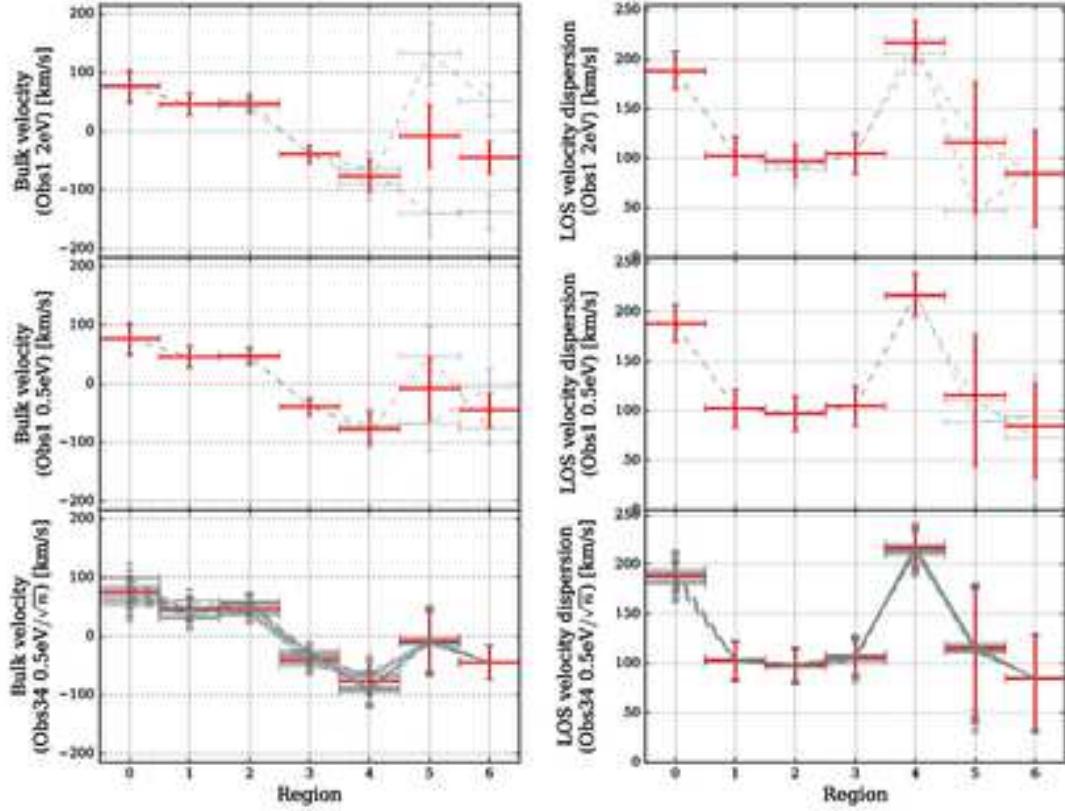


Fig. 12. The best-fitting bulk velocities and LOS velocity dispersions after manually shifting the energy gain. *Top:* the effect of the uncertainty of Obs 1 gain relative to Obs 3 and Obs 4. *Middle:* the effect of the pixel-to-pixel gain uncertainty within Obs 1. *Bottom:* the effect of the pixel-to-pixel gain uncertainties within Obs 3 and Obs 4. The red crosses are the best-fitting values shown in table 4, and the grey crosses and dashed lines represent the best-fitting values after the gain shifts.

A.2.1.1 Effect of the gain uncertainty

We investigated the effect of the gain uncertainty described in section 2.1 on the velocity measurements. We manually shifted the gain⁷ and followed the same velocity fitting described in section 3.2 to see how the result changes by the systematic gain difference. We shifted (1) the gain of all the Obs 1 data by ± 2 eV to account for the uncertainty of Obs 1 gain relative to Obs 3 and Obs 4 gain. (2) the gain of Reg 5 Obs 1 by ± 0.5 eV and at the same time the gain of Reg 6 Obs 1 by ∓ 0.5 eV for the pixel-to-pixel gain uncertainties within Obs 1. (3) the gain of Reg 0 Obs 3, Reg 0 Obs 4, Reg 1 Obs 3, Reg 1 Obs 4, Reg 2 Obs 3, Reg 2 Obs 4, Reg 3 Obs 3, Reg 3 Obs 4, Reg 4 Obs 3, and Reg 4 Obs 4 by $0.5 \text{ eV} / \sqrt{n}$, where n is the number of pixels of each single region, twenty times with random signs in each trial, for relative gain uncertainties within Obs 3 and Obs 4.

The best-fitting bulk velocities and LOS velocity dispersions after the above mentioned gain

⁷ We used `rmodel gain` command available in XSPEC, with `slope = 1` and `intercept = ΔE` where ΔE is the gain shift. We used the energy range of 6.4–6.7 keV.

shifts are shown in figure 12. We found in every case that the LOS velocity dispersion does not change significantly from the nominal value ($\lesssim 20 \text{ km s}^{-1}$ except for one case in Reg 5), although the best-fitting bulk velocity changes in proportion to the gain shifts.

A.2.2 Effect of the line spread function uncertainty

We examined the uncertainty of line spread function (LSF) of the SXS and its effect on the measurement of LOS velocity dispersion. Due to the incomplete state of the SXS calibration at the time of these observations, it is not possible to determine a robust estimate of the uncertainty on the instrumental broadening. In H16, we conservatively estimated the range of possible FWHM values as $5 \pm 0.5 \text{ eV}$ and set that as the 90% confidence level. This estimate was based on variation in the calibration pixel LSF over time, how the array resolution compared with the calibration-pixel resolution during the later calibration measurement, and the difference in apparent line widths between Obs 2 and Obs 3. Even this conservative value corresponded to a smaller uncertainty on the velocity broadening at the Fe He-alpha lines than that due to the statistical uncertainty. For the current paper, we would like to be able to use a less conservative value, and to assess the impact of both estimates on our results. For the more optimistic estimate, we have chosen $\pm 0.15 \text{ eV}$, based on the dispersion of the resolutions of the individual pixels across the array during the later in-orbit calibration with ^{55}Fe , and the premise that this dispersion represents pixel-dependent temporal variation more than intrinsic differences in the resolution.

The effect of its uncertainty on LOS velocity dispersion is expressed by

$$\Delta\sigma_v \simeq 3 \text{ km s}^{-1} \left(\frac{\sigma_v}{100 \text{ km s}^{-1}} \right)^{-1} \left(\frac{W_{\text{inst}}}{5 \text{ eV}} \right) \left(\frac{\Delta W_{\text{inst}}}{0.15 \text{ eV}} \right) \left(\frac{E_{\text{obs}}}{6.7 \text{ keV}} \right)^{-2}, \quad (\text{A1})$$

where W_{inst} is the FWHM of instrumental broadening and ΔW_{inst} is an uncertainty of instrumental broadening in FWHM, assuming $\Delta W_{\text{inst}} \ll W_{\text{inst}}$ (more details are shown in appendix of Kitayama et al. 2014). The effect is negligible.

A.2.3 Effect of the PSF shape uncertainty

We examined systematic uncertainties of LOS velocity dispersion introduced by the uncertainty of the PSF shape. As indicated in table 3, the cross-term contribution from Sky 0 to Reg 1 Obs 3 is the largest among cross-term contributions. We found that the difference is typically $\lesssim 5 \text{ km s}^{-1}$, except for Reg 1 ($\sim 10 \text{ km s}^{-1}$) even when this cross-term was changed by $\pm 30\%$, which is the maximum calibration uncertainty of the off-axis PSF normalizations between in the ground and in orbit (Maeda et al. 2017). We also checked the effect of PSF uncertainty on the results of Obs 1 (Reg 5 and Reg 6). By changing the contribution from Sky 2 by $\pm 30\%$ where is the largest contribution among the sky

regions, we found that the difference is $\sim 5 \text{ km s}^{-1}$, except for Reg 5 ($\sim 20 \text{ km s}^{-1}$).

A.2.4 Effect of the modeling uncertainty

We investigated the systematic uncertainty originating from plasma emission modeling. We examined the change of the best-fit redshift by fitting only Fe He α w line, which is not used in the velocity fitting in section 3.2. The analysis details are shown in appendix 3.3. This line has the highest counts among the He α complex. While the shape of this line can be affected by resonance scattering, the line centroid position is expected to be nearly unchanged. We obtained that the PSF-uncorrected bulk velocity of each regions are consistent between two methods except for in Reg 3 and Reg 6 (see table 7). The offset of bulk velocity in these two regions is $\lesssim 45 \text{ km s}^{-1}$. However, in Reg 6, when we modeled the w line using *bapec*, we obtained a consistent bulk velocity with that shown in table 4. This suggests that the discrepancy originates from the emission modelling uncertainties. The effect of the modeling uncertainty on the bulk velocity measurements is therefore $\lesssim 45 \text{ km s}^{-1}$.

Appendix 3 Details of velocity mapping

A.3.1 Accounting for PSF scattering

We now describe how we accounted for PSF scattering in section 3.2 in further detail. In the presence of steep X-ray surface brightness gradients, such as those in the cluster cool cores, the X-ray mirror PSF with a sharp core and broad wings (Okajima et al. 2016) can cause significant flux contamination from the bright cluster peak into the lower-brightness regions at distances much greater than the nominal HPD of 1.2 arcmin. It is therefore essential to take PSF scattering into account even if the regions of interest are much wider than ~ 1 arcmin.

To map the bulk velocities and velocity dispersions, we employ forward model fitting for pre-selected sky regions (as opposed to “backward” image deconvolution), adopting a method first used by Markevitch (1996) and Markevitch et al. (1996) to derive cluster temperature profiles and maps using *ASCA* data that was similarly affected by a broad PSF. We divided the Perseus core into seven sky regions (Sky 0 to Sky 6) as shown in figure 5 right. Their combined outline extends beyond the combined outline of the FOVs of the three SXS observations as described in section 3.2, in order to keep the scattered flux from *outside* that sky area into the FOV negligible, which is easily achieved given the cluster’s sharply declining X-ray brightness profile.

We assume that the X-ray emission in each sky region is represented by a single-temperature, single-velocity thermal plasma model M_j ($j = 0, 1, \dots, 6$). As the X-ray emission from each region passes thorough the X-ray telescope, it is spread among the detector pixels because of the PSF as well

as the slight drift of the satellite pointing direction during each observation. The spectra are collected in several detector regions shown in figure 5 left for each of the 3 observations. The detector regions are selected to follow the sky regions as close as possible, but because of the 0.5 arcmin pixel size and the pointing offsets, they are not the same for different observations. With Obs 1 covering only two sky Reg 5 and 6, we have a total of 12 spectra S_i ($i = 1, \dots, 12$) for all regions and all pointings. Each of those spectra is the sum of the contributions from all sky regions j :

$$S_i = R_i \sum_{j=0,6} P_{j \rightarrow i} M_j, \quad (\text{A2})$$

where $P_{j \rightarrow i}$ contains the relative flux contributions of the j -th sky region into the i -th detector region, and R_i is the spectral redistribution matrix for the i -th detector region.

To calculate these relative flux contributions, we use external data — Chandra ACIS images with a much better angular resolution. We combined Chandra ObsIDs 11713, 11714, 11715, 11716, 12025, 12033, 12036, 12037, 3209, 4289, 4946, 4947, 4948, 4949, 4950, 4951, 4952, 4953, 6139, 6145, and 6146, which include both ACIS-I and ACIS-S pointings. We used the standard Chandra data reduction techniques (see, e.g., Wang et al. 2016, for details), including subtracting the blank-sky background after normalizing it at high energies, and modeling and subtracting the CCD readout artifact. The central AGN is a bright X-ray source affected by pileup in the ACIS image, and for our current purposes of modeling the ICM emission, we masked the central source and replaced it with the average brightness for the adjacent pixels. Other areas of the image are not affected by pileup. Point sources other than the AGN were left in the image; their flux is negligible compared to the ICM emission. We constructed two images, one in the broad 1.8–9 keV energy band and another containing only the 6.7 keV line flux — to the accuracy possible with a CCD resolution. For the latter, we first extracted an image in the 6.4–6.7 keV band containing the redshifted 6.7 keV line complex (including the CCD line broadening). We then modeled the underlying continuum in this band by linear interpolation between images in the line-free intervals of 6.0–6.3 keV and 7.0–7.3 keV, with a small normalization correction to reflect the deviation of the spectrum from linear in this interval. The continuum image was then subtracted to result in a map of the 6.7 keV line emission.

These Chandra images were divided into the sky regions, the image for each region was then multiplied by the mirror effective area and vignetting and convolved with the PSF for each of the 3 Hitomi pointings and at each energy of interest (the effective area, vignetting and the PSF depend on the photon energy). For each of these sky region images j , the flux that falls into each of the detector regions i was collected. Technically, this was done using the Hitomi raytracing tool `aharfgen`, which generates an ARF containing the values $P_{j \rightarrow i}$ in the expression above. These values for the energy of the 6.7 keV line (redshifted), are given in table 3 as fractions of the sum for all regions.

In addition to the ICM emission, the spectra have a contribution from the central AGN scattered into each integration region. Therefore, a similar calculation of the scattered contributions for a point source representing the AGN was done as above. Its normalization is determined separately using the Hitomi data (AGN paper).

We can now derive the velocities and velocity dispersions for the 7 sky regions by fitting all 12 spectra simultaneously using the model S_i that includes the ICM and AGN components. This can be done using two different technical approaches, both of which we used in this work and described them in the following section.

A.3.2 The ARF method

In our main approach, whose results are described in section 3.2, the PSF effects are taken into account in XSPEC fitting by using the cross-region ARFs calculated as described above. This approach is general enough to allow fitting of various quantities such as temperatures and metallicities in addition to velocities. It also allows us to use different lines for velocity fitting — e.g., excluding the resonant (w) line and using only the remaining lines of the 6.76 keV complex unaffected by resonant scattering. Because the ARF values are applied by XSPEC to the APEC normalization (as opposed to model flux), the ARF should contain values calculated using an image of the projected emission measure rather than the X-ray brightness (Markevitch et al. 1996). Our broad-band Chandra image is an adequate approximation for this purpose. Furthermore, while the Chandra image contains information on the relative normalizations between various regions, given the calibration uncertainties, we let the overall model normalizations be free parameters for each spectrum. Thus we use external information only for the regions’ relative contributions into each spectrum. Fitting was done in 2 steps — first, temperatures were fit in a broad energy band excluding the 6.7 keV complex, then those temperatures were fixed, while the abundances and velocities were fit using the 6.7 keV complex (6.4–6.7 keV band excluding the w line). The best fit models and residuals for the velocity-fitting step of the above procedure are shown in figure 13.

To give a clearer idea of the procedure for joint fitting of 12 spectra with 8 model components (7 plasma models and an AGN model), we show below a part of the XSPEC command file used in the velocity fitting. Note that in the current XSPEC implementation, the spectral redistribution matrix (the ‘response’ commands below) is specified for each of the sky region contributions, even though it is the same file for all the components within the same spectrum and could be applied after summing the model components, as shown in eq. (A2) — this may change in the future.

```
# Spectrum 1 (observation 3, approximating sky region 0):
data 1 reg0obs3.pi
```

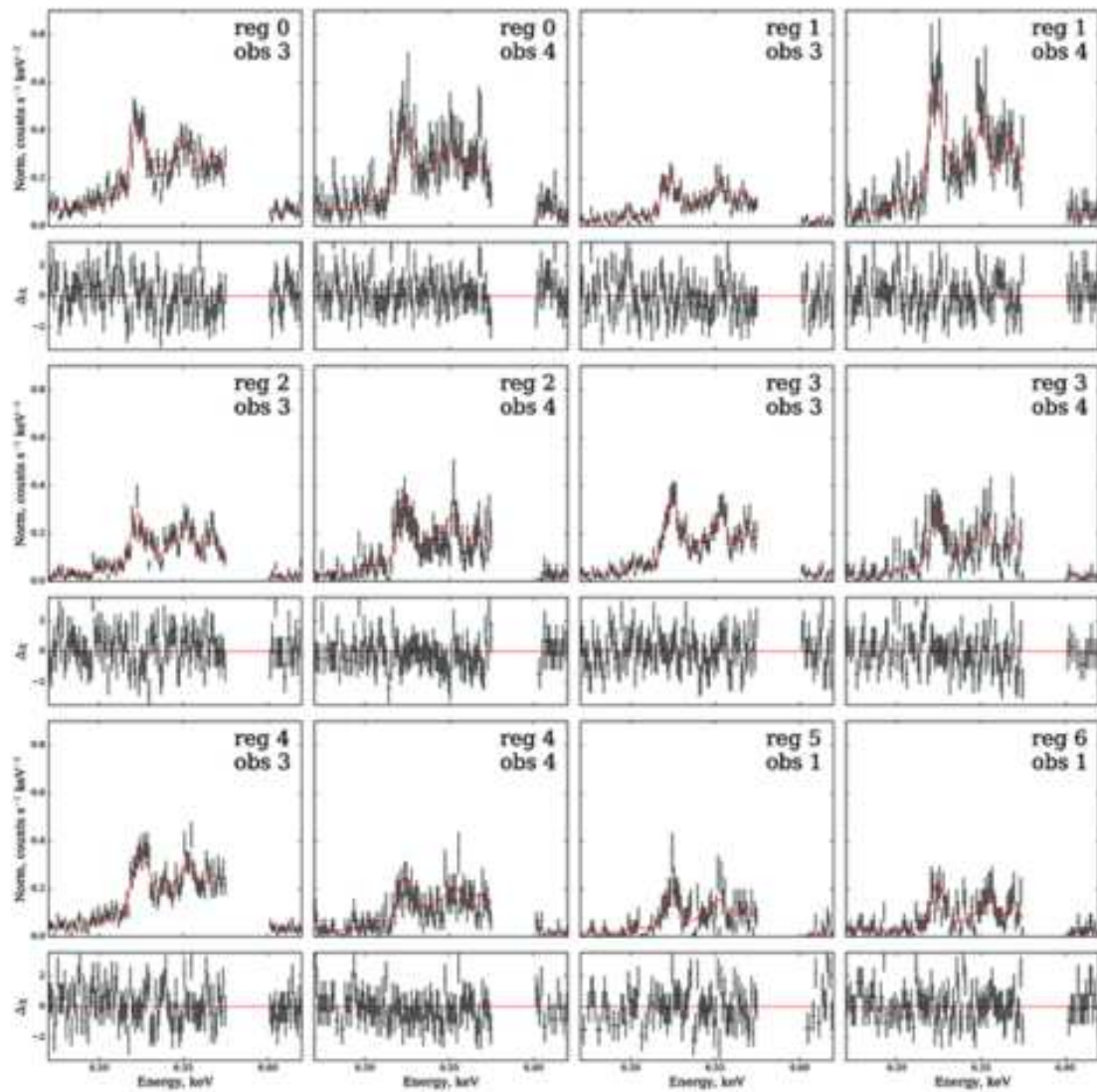


Fig. 13. Fits and residuals for the PSF-corrected velocity mapping.

```

# Contribution into this spectrum from the central point source:
response 1:1 reg0obs3.rmf
arf 1:1 AGN_reg0obs3.arf

# Contribution into this spectrum from sky region 0:
response 2:1 reg0obs3.rmf
arf 2:1 sky0_to_reg0obs3.arf

# Contribution into this spectrum from sky region 1:
response 3:1 reg0obs3.rmf
arf 3:1 sky1_to_reg0obs3.arf
...
response 8:1 reg0obs3.rmf
arf 8:1 sky6_to_reg0obs3.arf

```

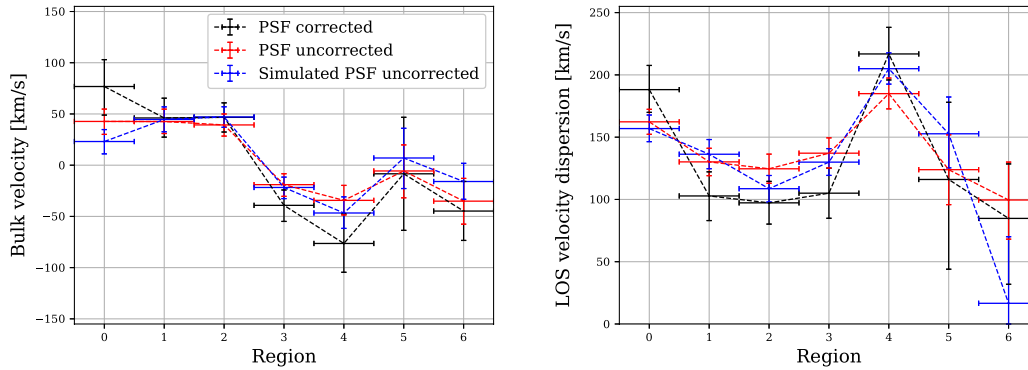


Fig. 14. Best-fit velocity and dispersion values for the sky regions. Black and red crosses show the PSF corrected and uncorrected fits to the real spectra, while blue crosses show the PSF-uncorrected fits to the simulated spectra, using the PSF-corrected values as input for the simulation. The agreement between blue and red crosses shows that the fitting method has found a self-consistent solution.

```

# Spectrum 2 (observation 4, approximating sky region 0):
data 2 reg0obs4.pi
...

# Spectrum 12 (observation 1, approximating sky region 6):
data 12 reg6obs1.pi
response 1:12 reg6obs1.rmf
arf 1:12 AGN_reg6obs1.arf
arf 2:12 sky0_to_reg6obs1.arf
...
arf 8:12 sky6_to_reg6obs1.arf

# Spectral models: component 1 for AGN, components 2-8 for sky regions 0-6:
model 1:agn TBabs(pegpurlw+zgauss+zgauss)
model 2:plasma0 TBabs*bapec
model 3:plasma1 TBabs*bapec
...
model 8:plasma6 TBabs*bapec

```

For a check of the results, we used the best-fit PSF-corrected values of the temperatures, abundances, velocities and dispersions, and applied the PSF blending (table 3) and detector response to generate simulated spectra for 12 detector regions. We then fitted the simulated spectra for individual regions (without the PSF correction, but simultaneously fitting the spectra for the same sky region from different pointings). We reproduced the fits for the real spectra within the statistical errors, as shown in figure 14.

A.3.3 Simplified velocity analysis using the w line

While the shape of the brightest (w) line of the He α triplet can be significantly affected by resonant scattering in the dense cluster core (which is indeed observed, see RS paper), the line centroid should

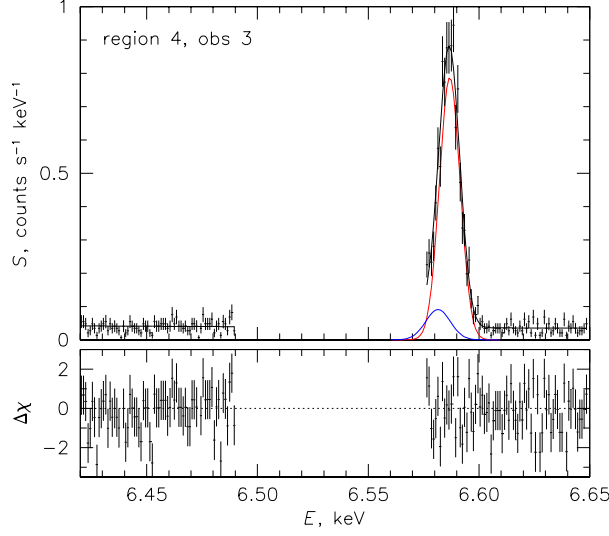


Fig. 15. A fit to the resonance line only, using a model consisting of a power law plus two Gaussians representing the resonance line (red curve) and a combination of its nearest satellites (blue curve). The other lines of the He α triplet are excluded from the fit. One spectrum is shown for illustration.

be less sensitive to scattering than its width. Thus, the w line can offer a useful test of the bulk velocity results derived above using the other lines of the triplet. Its width should also give an upper limit on turbulent broadening. This may be accomplished using the above ARF method, limiting the last step (fitting the velocities) to the narrow interval including only the w line. However, if we choose to fit only the w line, we can use a simpler and faster fitting approach, which is also less model-dependent, since it removes (to a good approximation) the effects of the dependence of the line flux ratios in the He α complex on the gas temperature.

To model the w line and the underlying continuum, we fit a Gaussian plus a power law in the energy intervals 6.42–6.49 keV and 6.575–6.65 keV (observer frame), see figure 15. The nearest bright component of the line complex, the x line, is 18 eV away from the w line (6.7004 keV rest frame) and is excluded using the above interval. However, there is a large number of faint satellites within $\Delta E = 10$ eV of the w component, which cumulatively account for 10–15% of the w flux (for a $T = 4$ keV plasma). If not included in the model, they would bias the w line position and width. We found that these satellites can be adequately modeled by adding one Gaussian component at $E = 6.695$ keV (rest frame) with an intrinsic width $\sigma = 3.7$ eV and an intensity 0.138 times that of the w line. To further simplify the model, we add in quadrature the typical expected velocity dispersion

of 160 km s^{-1} to this component, which gives a total width of $\sigma = 5.2 \text{ eV}$. While the satellite line fluxes depend on plasma temperature, and the velocity broadening is of course different in different spectra, this simplification proves to be adequate. Fitting simulated APEC spectra for a relevant range of plasma temperatures ($T = 3 - 5 \text{ keV}$) and velocity broadening ($\sigma_v = 100 - 200 \text{ km s}^{-1}$) using the above energy interval and a model consisting of a power law with a slope fixed at 5.0 (the local slope of the thermal spectrum for $T = 4 \text{ keV}$), the w line represented by a Gaussian with free redshift and width, and the satellite Gaussian with the width and relative flux fixed as above and the same redshift, we were able to recover the redshift to within 15 km s^{-1} and the line width to within 10 km s^{-1} . This redshift error is acceptable given the other uncertainties, e.g., $\sim 10 \text{ km s}^{-1}$ systematic uncertainty due to the difference between the measured (e.g. Beiersdorfer et al. 1993) and theoretical (Atomic paper) w line energies of up to $\sim 0.3 \text{ eV}$. A fit to one of the spectra is shown in figure 15, where red shows the w component and blue the satellite component. Freeing the slope of the power law does not affect the best-fit line parameters, because with our choice of the energy intervals, the continuum fit straddles the line. We also verified that fits to the real spectra using this model or full APEC in the same energy interval agree within the above errors.

We model each of the 12 spectra with a sum of 6 two-Gaussian models (one for each sky region) constructed as above. Redshifts and velocity dispersions for each sky region are tied between the 12 spectra, and the relative normalizations of the 6 main Gaussians within each spectrum are fixed to the PSF-scattered fractions given in table 3. Here we use the fractions computed using the Chandra image of the 6.7 keV line emission (see above), which are directly applicable to our Gaussian line normalizations. Thus, instead of using 6 ARFs for each spectrum to represent the PSF contributions from each of the 6 regions, as is done in our main method (section 3.2), in this method we account for the PSF mixing within the model for each spectrum. We use only one ARF and RMF for each spectrum (we used an ARF generated for a point source in the middle of each region, but it does not matter). For reasons related to XSPEC technical implementation, this fitting method is much faster — provided the approximations used in it are acceptable. As in the ARF method (section 3.2), we allow the overall model normalization for each spectrum to be a free parameter (even though the normalizations for each sky region can be computed from the Chandra image) to account for calibration uncertainties. The power law component for each spectrum, which represents the sum of the thermal continuum and the AGN contribution, was allowed to be a free parameter, because we are interested in the line components only and must model the underlying continuum well. It is also possible to use APEC as a model for the w line, using the same relative model normalization scheme (though care should be taken to apply the PSF mixing fractions to *line fluxes* rather than the APEC normalizations), but it is much slower.

A subset of XSPEC commands for this method and a printout of the model for one of 12 spectra are given below to provide a clearer view of the procedure.

```

# Spectrum 1 (observation 3, approximating region 0):
data 1:1 reg0_obs3_HP_gr1.pi
response 1:1 reg0_obs3_HP_l.rmf
arf 1:1 reg0_obs3_HP_ps1890.arf

# Spectrum 2 (observation 4, approximating region 0):
data 1:2 reg0_obs4_HP_gr1.pi
response 2:2 reg0_obs4_HP_l.rmf
arf 2:2 reg0_obs4_HP_ps1890.arf
...
# Spectrum 12 (observation 1, approximating region 6)
data 1:12 reg6_obs1_HP_gr1.pi
response 12:12 reg6_obs1_HP_l.rmf
arf 12:12 reg6_obs1_HP_ps1890.arf

# Model for spectrum 1: a pair of Gaussians (a w line and the sum of the
# nearby satellites with a normalization 0.138*w) for each of the 7 sky
# regions, plus a power law:
model 1:reg03 zgauss + zgauss + zgauss + zgauss + zgauss + zgauss + zgauss
          + zgauss + zgauss + zgauss + zgauss + zgauss + zgauss + zgauss
          + powerlaw

# Printout of the model for one spectrum (reg03), showing parameter
# dependencies. The normalization of the 'diagonal' (i=j) Gaussian
# (parameter 4 for this spectrum) is free, while normalizations of the
# w components from other sky regions are tied to it via the relative
# PSF contributions (for simplicity we use 0 for the fractions <5%):
  1   1   zgauss   LineE   keV   6.70040   frozen
  2   1   zgauss   Sigma   keV   5.41827E-03 +/- 4.01105E-04
  3   1   zgauss   Redshift          1.76995E-02 +/- 5.97538E-05
  4   1   zgauss   norm              5.19561E-05 +/- 1.72050E-06
  5   2   zgauss   LineE   keV   6.69500   frozen
  6   2   zgauss   Sigma   keV   5.20000E-03 frozen
  7   2   zgauss   Redshift          1.76995E-02 = reg03:p3
  8   2   zgauss   norm              7.16994E-06 = reg03:p4*0.138
  9   3   zgauss   LineE   keV   6.70040   frozen
 10   3   zgauss   Sigma   keV   3.39663E-03 +/- 2.76307E-04
 11   3   zgauss   Redshift          1.74271E-02 +/- 4.28597E-05
 12   3   zgauss   norm              8.41689E-06 = reg03:p4*0.162
 13   4   zgauss   LineE   keV   6.69500   frozen
 14   4   zgauss   Sigma   keV   5.20000E-03 frozen
 15   4   zgauss   Redshift          1.74271E-02 = reg03:p11
 16   4   zgauss   norm              1.16153E-06 = reg03:p12*0.138
 17   5   zgauss   LineE   keV   6.70040   frozen
 18   5   zgauss   Sigma   keV   3.48743E-03 +/- 2.36872E-04
 19   5   zgauss   Redshift          1.75454E-02 +/- 3.76188E-05
 20   5   zgauss   norm              1.15343E-05 = reg03:p4*0.222
 21   6   zgauss   LineE   keV   6.69500   frozen
 22   6   zgauss   Sigma   keV   5.20000E-03 frozen
 23   6   zgauss   Redshift          1.75454E-02 = reg03:p19

```


24	6	zgauss	norm		1.59173E-06	= reg03:p20*0.138
25	7	zgauss	LineE	keV	6.70040	frozen
26	7	zgauss	Sigma	keV	4.65027E-03	+/- 2.67985E-04
27	7	zgauss	Redshift		1.71175E-02	+/- 4.26310E-05
28	7	zgauss	norm		6.18277E-06	= reg03:p4*0.119
29	8	zgauss	LineE	keV	6.69500	frozen
30	8	zgauss	Sigma	keV	5.20000E-03	frozen
31	8	zgauss	Redshift		1.71175E-02	= reg03:p27
32	8	zgauss	norm		8.53223E-07	= reg03:p28*0.138
33	9	zgauss	LineE	keV	6.70040	frozen
34	9	zgauss	Sigma	keV	3.95278E-03	+/- 2.31365E-04
35	9	zgauss	Redshift		1.71612E-02	+/- 3.71691E-05
36	9	zgauss	norm		5.09170E-06	= reg03:p4*0.098
37	10	zgauss	LineE	keV	6.69500	frozen
38	10	zgauss	Sigma	keV	5.20000E-03	frozen
39	10	zgauss	Redshift		1.71612E-02	= reg03:p35
40	10	zgauss	norm		7.02654E-07	= reg03:p36*0.138
41	11	zgauss	LineE	keV	6.70040	frozen
42	11	zgauss	Sigma	keV	4.61808E-03	+/- 6.04779E-04
43	11	zgauss	Redshift		1.73606E-02	+/- 9.80638E-05
44	11	zgauss	norm		0.0	= reg03:p4*0.
45	12	zgauss	LineE	keV	6.69500	frozen
46	12	zgauss	Sigma	keV	5.20000E-03	frozen
47	12	zgauss	Redshift		1.73606E-02	= reg03:p43
48	12	zgauss	norm		0.0	= reg03:p44*0.138
49	13	zgauss	LineE	keV	6.70040	frozen
50	13	zgauss	Sigma	keV	3.92239E-03	+/- 4.30404E-04
51	13	zgauss	Redshift		1.70599E-02	+/- 6.30424E-05
52	13	zgauss	norm		0.0	= reg03:p4*0.
53	14	zgauss	LineE	keV	6.69500	frozen
54	14	zgauss	Sigma	keV	5.20000E-03	frozen
55	14	zgauss	Redshift		1.70599E-02	= reg03:p51
56	14	zgauss	norm		0.0	= reg03:p52*0.138
57	15	powerlaw	PhoIndex		5.00000	frozen
58	15	powerlaw	norm		7.22371	+/- 0.208572

In models for other spectra, redshifts and widths of the lines are
tied to the values for the respective sky region in this model.
A total of 38 parameters are being fit.

The resulting LOS velocities (in the same reference frame as above) and velocity dispersions are given in table 7. It gives both the individual, PSF-uncorrected fits for each sky region (fitting together either two or one spectra for each region, as above) and the joint PSF-corrected fit to all spectra. The joint fit is good, with C statistic of 1390 for 1484 d.o.f. Residuals for individual spectra are shown in figure 16.

We note that these velocities and dispersions are derived using both a different fitting method and the independent data excluded from our main fit. It thus provides a good check of that fit. The PSF-corrected velocities from both methods are in good statistical agreement and show the same large-scale velocity gradient. The velocity dispersions from the w line method show approximately

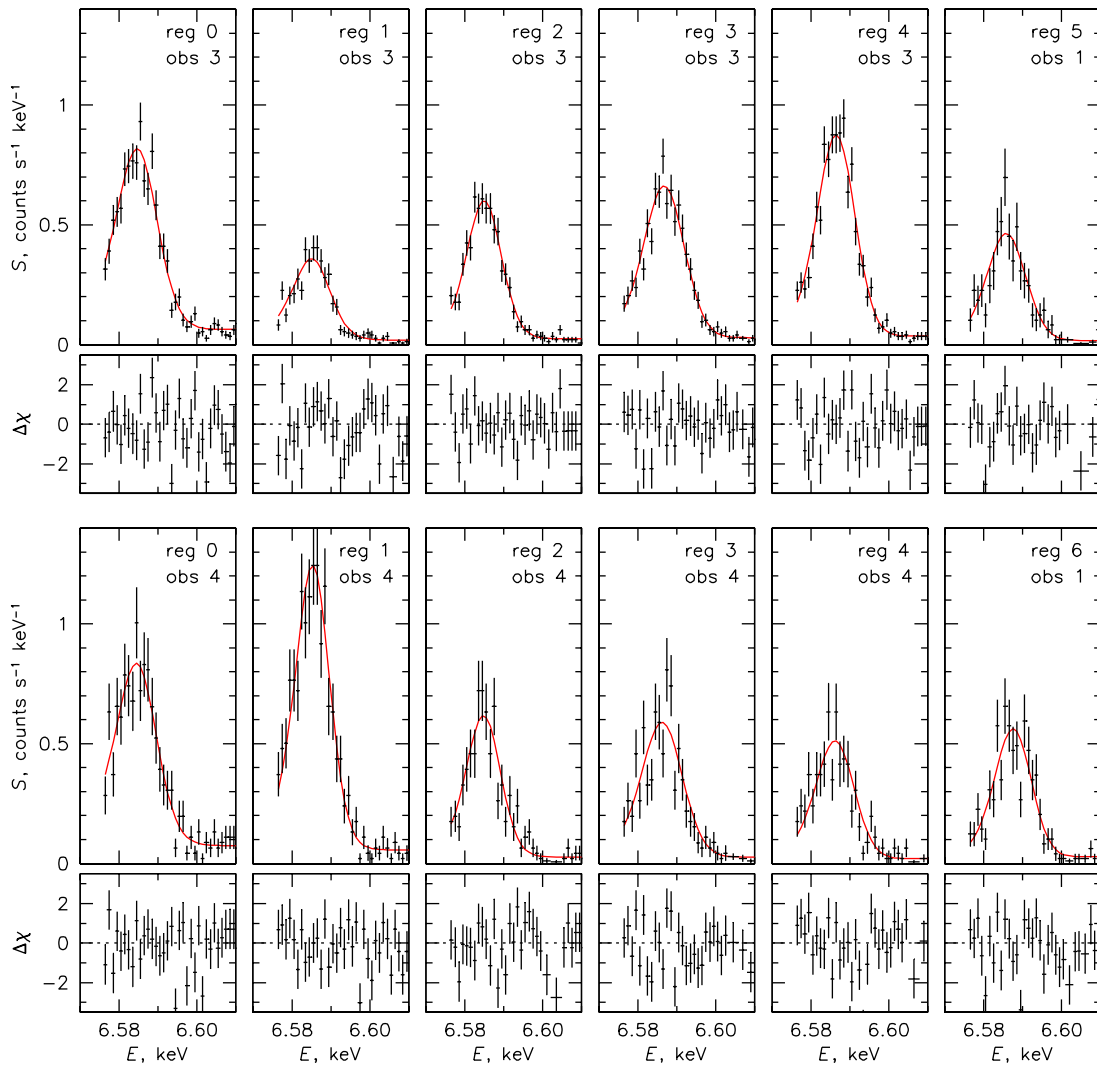


Fig. 16. Fits and residuals for the joint fit of all spectra using the w -line method (figure 15). The continuum energy interval to the left of the line complex (see figure 15) is not shown.

Table 7. Best-fit bulk velocity and LOS velocity dispersion values. Values of v and σ_v are km s^{-1} .

region	w line excluded, ARF method				Fit w line only, model mixing method			
	PSF uncorrected		PSF corrected		PSF uncorrected		PSF corrected	
	v_{bulk}	σ_v	v_{bulk}	σ_v	v_{bulk}	σ_v	v_{bulk}	σ_v
0	43^{+12}_{-13}	163^{+10}_{-10}	75^{+26}_{-28}	189^{+19}_{-18}	50^{+8}_{-8}	194^{+9}_{-8}	98^{+20}_{-18}	228^{+21}_{-20}
1	42^{+12}_{-12}	131^{+11}_{-11}	46^{+19}_{-19}	103^{+19}_{-20}	33^{+8}_{-8}	163^{+9}_{-9}	16^{+13}_{-13}	127^{+17}_{-16}
2	39^{+11}_{-11}	126^{+12}_{-12}	47^{+14}_{-14}	98^{+17}_{-17}	39^{+8}_{-7}	158^{+9}_{-9}	52^{+11}_{-12}	132^{+15}_{-14}
3	-19^{+11}_{-11}	138^{+12}_{-12}	-39^{+15}_{-16}	106^{+20}_{-20}	-43^{+8}_{-8}	193^{+9}_{-8}	-76^{+13}_{-13}	191^{+16}_{-16}
4	-35^{+15}_{-14}	186^{+12}_{-12}	-77^{+29}_{-28}	218^{+21}_{-21}	-30^{+7}_{-7}	175^{+8}_{-7}	-63^{+11}_{-11}	156^{+14}_{-14}
5	-6^{+25}_{-26}	125^{+28}_{-28}	-9^{+55}_{-56}	117^{+62}_{-73}	-9^{+17}_{-17}	175^{+20}_{-18}	-3^{+30}_{-29}	189^{+37}_{-35}
6	-35^{+22}_{-22}	99^{+31}_{-32}	-45^{+29}_{-29}	84^{+44}_{-54}	-78^{+15}_{-15}	164^{+17}_{-16}	-93^{+19}_{-19}	154^{+21}_{-20}

similar spatial pattern, but most values are higher (though they are statistically inconsistent only in Reg 3). Higher widths for the w line are expected in the presence of resonant scattering. We also fit the w line in the same energy interval using the ARF method and obtained results very close to those from the simplified method.

A.3.4 Velocity analysis using $\text{He}\beta$ lines

Fe $\text{He}\beta$ lines are optically thin and thus provide another consistency check of our main result in section 3.2. We focused our comparison only on the PSF uncorrected σ_v values, because the statistics of the $\text{He}\beta$ lines is not as good as that of the $\text{He}\alpha$ complex and the gain is not well calibrated compared to the $\text{He}\alpha$ complex.

We fit the spectra in the energy range of 7.7–7.8 keV or 7.6–7.9 keV (observer frame) using *bapec*, with all parameters allowed to vary. The narrower energy range includes only the $\text{He}\beta$ lines and the results are not significantly affected by other lines. The results obtained using the wider energy range are not as clean as the former ones, because the energy range also covers the Ni $\text{He}\alpha$ line, but the errorbars are small because of the higher statistics for the continuum determination. As in above PSF-uncorrected fits, we fit spectra from different sky regions independently, while fitting simultaneously the spectra for the same sky region from different pointings.

The resulting best-fit σ_v are shown in table 8. The PSF-uncorrected σ_v values obtained from the optically thin lines ($\text{He}\alpha$ $x+y+z$ or $\text{He}\beta$) are consistent with each other.

Table 8. Best-fit LOS velocity dispersion (σ_v) in the unit of km s^{-1} .

	He α , w excluded	He β , 7.7–7.8 keV	He β , 7.6–7.9 keV
0	163^{+10}_{-10}	145^{+36}_{-32}	160^{+31}_{-29}
1	131^{+11}_{-11}	112^{+31}_{-112}	109^{+25}_{-26}
2	126^{+12}_{-12}	95^{+62}_{-83}	154^{+30}_{-28}
3	138^{+12}_{-12}	152^{+31}_{-32}	138^{+31}_{-30}
4	186^{+12}_{-12}	196^{+27}_{-25}	184^{+24}_{-23}
5	125^{+28}_{-28}	42^{+128}_{-42}	151^{+96}_{-77}
6	99^{+31}_{-32}	96^{+95}_{-96}	171^{+70}_{-79}